



LAWRENCE
LIVERMORE
NATIONAL
LABORATORY

The Madden-Julian Oscillation in ECHAM4/4.6 Coupled and Uncoupled GCMs

K. R. Sperber, G. Gualdi, S. Legutke, V. Gayler

July 27, 2004

Climate Dynamics

Disclaimer

This document was prepared as an account of work sponsored by an agency of the United States government. Neither the United States government nor Lawrence Livermore National Security, LLC, nor any of their employees makes any warranty, expressed or implied, or assumes any legal liability or responsibility for the accuracy, completeness, or usefulness of any information, apparatus, product, or process disclosed, or represents that its use would not infringe privately owned rights. Reference herein to any specific commercial product, process, or service by trade name, trademark, manufacturer, or otherwise does not necessarily constitute or imply its endorsement, recommendation, or favoring by the United States government or Lawrence Livermore National Security, LLC. The views and opinions of authors expressed herein do not necessarily state or reflect those of the United States government or Lawrence Livermore National Security, LLC, and shall not be used for advertising or product endorsement purposes.

The Madden–Julian Oscillation in ECHAM4 Coupled and Uncoupled General Circulation Models

K. R. Sperber

Program for Climate Model Diagnosis and Intercomparison, Lawrence Livermore National Laboratory, P.O. Box 808, L-103, Livermore, CA 94550, USA

E-mail: sperber1@llnl.gov Tel.: +1-925-4227720

Fax: +1-925-4227675

S. Gualdi

National Institute of Geophysics and Volcanology, Via Gobetti 101, 40129, Bologna, Italy

S. Legutke and V. Gayler

Models and Data Group,

Max Planck Institute of Meteorology, Bundesstrasse 58, 20146, Hamburg, Germany

Climate Dynamics

(Revised)

Abstract

The Madden-Julian oscillation (MJO) dominates tropical variability on timescales of 30–70 days. During the boreal winter/spring, it is manifested as an eastward propagating disturbance, with a strong convective signature over the eastern hemisphere. The space–time structure of the MJO is analyzed using simulations with the ECHAM4 atmospheric general circulation model run with observed monthly mean sea- surface temperatures (SSTs), and coupled to three different ocean models. The coherence of the eastward propagation of MJO convection is sensitive to the ocean model to which ECHAM4 is coupled. For ECHAM4/ OPYC and ECHO-G, models for which ~100 years of daily data is available, Monte Carlo sampling indicates that their metrics of eastward propagation are different at the 1% significance level. The flux-adjusted coupled simulations, ECHAM4/OPYC and ECHO-G, maintain a more realistic mean-state, and have a more realistic MJO simulation than the non-adjusted scale interaction experiment (SINTEX) coupled runs. The SINTEX model exhibits a cold bias in Indian Ocean and tropical West Pacific Ocean SST of ~0.5°C. This cold bias affects the distribution of time-mean convection over the tropical eastern hemisphere. Furthermore, the eastward propagation of MJO convection in this model is not as coherent as in the two models that used flux adjustment or when compared to an integration of ECHAM4 with prescribed observed SST. This result suggests that simulating a realistic basic state is at least as important as air–sea interaction for organizing the MJO. While all of the coupled models simulate the warm (cold) SST anomalies that precede (succeed) the MJO convection, the interaction of the components of the net surface heat flux that lead to these anomalies are different over the Indian Ocean. The ECHAM4/OPYC model in which the atmospheric model is run at a horizontal resolution of T42, has eastward propagating zonal wind anomalies and latent heat flux anomalies. However, the integrations with ECHO-G and SINTEX, which used T30 atmospheres, produce westward propagation of the latent heat flux anomalies, contrary to reanalysis. It is suggested that the differing ability of the models to represent the near-surface westerlies over the Indian Ocean is related to the different horizontal resolutions of the atmospheric model employed.

The Madden–Julian oscillation (MJO) is the dominant mode of subseasonal variability during the boreal winter/spring (Madden and Julian 1971, 1972, 1994). Over the tropical eastern hemisphere, the MJO controls convection on timescales of 30–70 days, and during years when the MJO is strong, reduced seasonal monsoon rainfall tends to occur over northern/central Australia (Hendon et al. 1999). Owing to the large-scale nature and temporal persistence of the convection, extratropical teleconnections have been noted (e.g., Weickmann et al. 1985; Murakami 1988) including an influence on rainfall over the western US (Mo and Higgins 1998; Higgins et al. 2000). Ferranti et al. (1990) found an enhancement of skill in extra-tropical medium- and extended-range numerical weather prediction when the MJO was included in the forecasts. Additionally, the MJO and associated westerly wind bursts have been shown to affect the development of the El Niño/Southern Oscillation through the generation of downwelling Kelvin waves that modify the vertical structure of the ocean heat content (McPhaden 1999, 2004). Given the near-global extent of its influence, as well as the variety of time scales that it affects, the MJO is an important mode of variability to simulate in weather, seasonal forecast, and climate models.

The simulation of the MJO remains a challenge to the modelers. Typical MJO errors in climate models include a weak amplitude, too short of a period, and lack of coherent propagation from the Indian Ocean into the Pacific (e.g., Slingo et al. 1996; Sperber et al. 1997). Slingo et al. (1996) suggested that convection schemes closed on buoyancy rather than large-scale moisture convergence might result in a more realistic MJO simulation. Tokioka et al. (1988) and Wang and Schlesinger (1999) showed that the propagation characteristics of the MJO were sensitive to the details of the convection scheme. Inness et al. (2001) found that increased vertical resolution gave a more realistic representation of the trimodal distribution of tropical clouds, and an improved MJO. Sperber et al. (1997) and Flatau et al. (1997) suggested that air–sea interaction was also important. Numerical experiments by Waliser et al. (1999) showed that inclusion of air–sea interaction gave rise to stronger and more coherent eastward propagation relative to a simulation forced with prescribed sea-surface temperatures (SST). However, surface flux errors in the coupled system can compromise the MJO (Hendon 2000). Inness et al. (2003) and Inness and Slingo (2003) demonstrated that even in the presence of air–sea interaction, a well-simulated basic state is crucial for MJO simulation. Evaluation of component models have reinforced the importance of air–sea interaction for the representation of the MJO. Using a 1-D mixed layer model, Shinoda and Hendon (1998) showed that SST anomalies consistent with observations could be obtained when the model was forced with surface fluxes derived from the Tropical Ocean Global Atmosphere Coupled Ocean–Atmosphere Response Experiment bulk flux algorithm (Fairall et al. 1996). Woolnough et al. (2001) captured many aspects of response of the atmosphere to idealized intraseasonal SST forcing, including convection lagging the positive SST anomalies and a westward vertical tilt of moisture and winds. However, they noted that “the aqua-planet model has surface easterlies at the equator, in contrast to the westerlies

required for the proposed coupled mechanism to work.’’ Later, Matthews (2004) found that the atmospheric response to prescribed observed pentad SST was too fast, and that the surface fluxes generated would act to damp the intraseasonal SST anomalies. Additionally, the convection anomalies did not lag the SST anomalies with the correct time scale. Thus, the above results suggest that air–sea interaction and a good basic state are necessary (though not sufficient) conditions for obtaining a realistic MJO.

Numerous studies of MJO with different versions of the ECHAM atmospheric model have been performed. Gualdi et al. (1997) analyzed the MJO in ECHAM2 and ECHAM3 with prescribed climatological SST. EC- HAM3 gave a more realistic distribution of MJO convection and its relation to the 200 hPa zonal wind than ECHAM2, in which the anomalies were also much weaker. They suggested that the improvement was due to a better representation of the tropical circulation with the incorporation of the Tiedtke (1989) convection scheme. However, they found that ECHAM3 intraseasonal convection was substantially overestimated over Central/South America at horizontal resolutions of T42 and higher. Subsequently, Gualdi and Navarra (1998) demonstrated further improvement in the MJO simulation when the closure of the Tiedtke (1989) convection scheme was replaced by a buoyancy criterion (Nordeng 1994) by comparing ECHAM4 with ECHAM3. Later, Gualdi et al. (1999) used ECHAM4 at T30 horizontal resolution with observed SST for 1980–1993 to study MJO modulation by ENSO. Using ensembles of integrations, they found that MJO convection extended east (was confined west) of the dateline during El Nino (La Nina). Kemball-Cook et al. (2002) found that ECHAM4 coupled to a 2.5 layer intermediate ocean model was able to represent low-level moisture convergence in advance of the convection, consistent with the current paradigm of the MJO evolution. Importantly, the convection was more coherent in the coupled simulation compared to an AMIP-type run. Contrary to this result, Liess et al. (2004) found that intraseasonal variability in the EC- HAM4/OPYC coupled model, the same version used herein, was less well represented compared to an AMIP- type simulation with the ECHAM4 AGCM. They based their analysis on 200 hPa velocity potential, from which composites of OLR and SST were made, and all seasons were included in the analysis.

The purpose of this paper is to analyze the boreal winter MJO in ECHAM4 when it is coupled to a variety of different ocean models and when forced with observed monthly mean SST. In addition to the spatial structures typically analyzed in modelling studies (e.g., OLR, rainfall, wind, and SST), we also analyze the vertical structure of the humidity and divergence, which show well-defined lead-lag structures relative to the MJO convection, as discussed in Sperber (2003). The methodology is the same as in Sperber (2004a), in which the MJO was analyzed in the National Center for Atmospheric Research Community Atmospheric Model 2.0 and the Community Coupled System Model 2.0.

2 Models and validation data

2.1 The models

The ECHAM4 atmospheric general circulation model (AGCM) is run with two different observed monthly mean SST datasets, and is also coupled to three different ocean models. Table 1 contains basic information with regard to the experiment notation and model configurations used in this paper. The AGCM has 19 hybrid sigma coordinate vertical levels extending from the surface to 10 hPa. The convection scheme is that of Tiedtke (1989), with the closure modified to be closed on buoyancy rather than large-scale moisture convergence (Nordeng 1994). Further details of the atmospheric model are described in Roeckner et al. (1996). In the prescribed SST run using the Hadley Centre Ice and Sea Surface Temperature dataset (HadISST; Rayner et al. 2000), and in all of the coupled simulations, the standard physics is used. However, for the simulation that used the Atmospheric Model Intercomparison Project (AMIP) II SST and sea ice (predominantly based on Reynolds and Smith 1994), a different physics option was invoked. This option changes the Charnock constant, parameters for the vertical diffusion and surface scheme as well as the cloud parameterization, the specification of sea-ice thickness, and uses an alternative ozone dataset. Differences in the climatology of SST between the AMIP II and HadISST datasets are typically less than 0.15°C over the Indian Ocean and western/central Pacific Ocean. The ECHAM4/AMIP II run was performed at T42 ($\sim 2.8^{\circ}$ – $\sim 2.8^{\circ}$) horizontal resolution, while the ECHAM4/HadISST run used T30 ($\sim 3.75^{\circ}$ – $\sim 3.75^{\circ}$). In terms of monthly mean climate statistics, Stendel and Roeckner (1998) have shown that the T30 and T42 version of the AGCM give comparable performance. For such metrics, comparison between ECHAM4/AMIP II and ECHAM4/HadISST most likely reflects the differences in the physics of the AGCM, though the choice of ozone data may contribute to differences in the simulation. The possible role that horizontal resolution plays in the representation of the MJO is discussed in Sect. 3.3.

In ECHAM4/OPYC, the AGCM was run at a horizontal resolution of T42. The ocean general circulation model (OGCM), version 3 of OPYC (Ocean and isoPYCnal coordinate), was also run at T42, but equator-ward of 36° the meridional resolution gradually increases to 0.5° to better resolve the equatorial ocean wave dynamics. OPYC utilizes an isopycnal coordinate system with 11 vertical levels. Near the ocean surface, where turbulence is important, a free surface mixed layer model is coupled to the isopycnal model. On the basis of the turbulent kinetic and mean potential energy, entrainment/detrainment across the isopycnal surface is calculated. Annual mean flux adjustments of heat and freshwater are determined from a 100-year spin-up of the coupled model. These artificial constraints minimize drift of the coupled climate system and help maintain a realistic basic state. Further details of OPYC have been described in Oberhuber (1993a, b).

In ECHO-G, the AGCM was run at a horizontal resolution of T30. The OGCM, the global Hamburg Ocean primitive equation model (HOPE-G), was run at T42. Equatorward of $\pm 30^{\circ}$ the

meridional resolution is gradually increased to 0.5° within 10° of the equator to better resolve the equatorial wave guide. The ocean model has 20 vertical levels, eight of which are in the upper 200 m, with a free surface. The atmospheric and ocean GCMs exchange information once a day via the ocean atmosphere sea-ice soil (OASIS) coupler (Legutke and Voss 1999, Valcke et al. 2000). Prior to coupling, the atmosphere (ocean) model was integrated for 18 (2034) years. After coupling, the last 100 years of a 155- year spin-up were used to determine annual mean flux adjustments for heat and freshwater fluxes. Further details of the ocean model can be found in Legutke and Maier-Reimer (1999), and the performance of ECHO-G is presented in Min et al. (2004).

The scale interaction experiment (SINTEX) coupled model uses the ECHAM4 AGCM at T30 horizontal resolution, and the Ocean Parallelized (OPA) 8.1 OGCM is on a $2.0^\circ \times 1.5^\circ$ grid, but equatorward of $\sim 19^\circ$ the meridional resolution gradually increases to 0.5° within $\sim 2.5^\circ$ of the equator. There are 31 levels in the vertical, 10 of which are located in the upper 100 m. Lateral mixing of temperature and salinity is “quasi-pure” isopycnal as described by Guilyardi et al. (2001), and the model has a rigid lid. The ocean and atmosphere model exchange information every 3 h via the OASIS coupler. Further details of the ocean model can be found in Madec et al. (1998). Aspects of the SINTEX model’s interannual variability over the Indian and Pacific Oceans can be found in Gualdi et al. (2003) and Guilyardi et al. (2003), respectively.

The integrations of ECHAM4 with the prescribed SST and sea ice span the period 1979–1995, corresponding to the base period of the AMIP II experiment. In these runs, 16 boreal winters are analyzed. For the coupled models, the detailed analysis of MJO was performed using 19 winters of data from control (present-day) integrations. The ECHAM4/OPYC and ECHO-G data were taken from the end of the integrations submitted to the Coupled Model Intercomparison Project 2+ (CMIP2+) database at the Program for Climate Model Diagnosis and Intercomparison (PCMDI). These data were analyzed as part of an appraisal of the mean state and variability of the CMIP2+ models (AchutaRao et al. 2004). Additionally, for these two models, upwards of 100 years of data were available, and outgoing longwave radiation (OLR) using the longer record was also analyzed to test the robustness of the metrics used to characterize the eastward propagation of convection. For the SINTEX model, two simulations from different initial conditions were analyzed. All of the results are based on the calendar months, November– March, when the MJO tends to be strongest.

Subseasonal variations of rainfall are characterized using the climate prediction center merged analysis of precipitation (CMAP). This dataset uses essentially the same algorithm and data sources as the monthly CMAP dataset described by Xie and Arkin (1997). The version used is based on a blend of gauge data with satellite products, including GPI (GOES precipitation index based on geostationary infrared data), microwave sounding unit (MSU), OLR-based precipitation index (OPI), special sensor microwave/imager (SSM/I) scattering, and SSM/I emission.

2.2 Validation data

The NCEP/NCAR reanalysis was a joint project between NCEP and NCAR to produce a multidecadal record of global atmospheric analyses with a fixed data assimilation system (Kalnay et al. 1996). The data assimilation and forecast model were implemented operationally at NCEP in January 1995. The model is run at a horizontal resolution of T62 and with 28 vertical levels. Moist convection is represented by a simplified Arakawa–Schubert parametrization scheme (Pan and Wu 1994), and clouds are diagnosed using a scheme based on Slingo (1987). Data were assimilated using a spectral statistical interpolation/3-D variational analysis method that requires no nonlinear normal mode initialization. Upper air data on standard pressure surfaces have been supplied on a 2.5° latitude/ longitude grid. Surface and 24-h forecast fields (e.g., fluxes) are on the equivalent T62 Gaussian grid. The spin-up of the hydrological cycle is small in the NCEP/ NCAR reanalysis (e.g., Mo and Higgins 1996; Stendel and Arpe 1997). For the period analyzed herein, the optimally interpolated sea-surface temperature (SST) of Reynolds and Smith (1994) were linearly interpolated to daily values.

3 The Madden–Julian oscillation

3.1 Time mean state and intraseasonal variance

The observed time–mean OLR for November–March, shown in Fig. 1a, indicates that deep convection from the central Indian Ocean to the central Pacific is collocated with the warm pool. The ECHAM4/AMIP II model underestimates the OLR over the western/central Pacific Ocean, while too much longwave radiation escapes to space over the Indian Ocean (Fig. 1b). In ECHAM4/HadISST (Fig. 1c), the convection over the Indian Ocean is stronger despite the SST being $0.1\text{--}0.15^\circ\text{C}$ colder compared to ECHAM4/AMIP II. The ECHAM4/OPYC OLR climatology, seen in Fig. 1d, closely resembles that of ECHAM4/HadISST. However, in both of these models, the convection is too weak in the vicinity of the Maritime Continent. ECHO-G tends to be more consistent with observations in that the pattern of convection is more coherent over the tropical eastern hemisphere (Fig. 1e), though it is weak compared to observations. The SINTEX simulations did not utilize flux adjustment, and as such the SST is $\sim 0.5\text{--}1^\circ\text{C}$ too cold over the Indian Ocean, and the warm pool is not as extensive in the western Pacific. Over these regions, the convection is weak compared to observations, with the main center of convection located over the Maritime continent.

Figure 2 shows the November–March 850 hPa wind climatology, which has proven to be a good indicator of the easternmost longitude to which MJO convection propagates (Inness et al. 2003). In the reanalysis (Fig. 2a), the tropical westerlies tend to be collocated with the strongest convection over the Pacific Ocean (Fig. 1a). Of the coupled models, ECHAM4/OPYC has the

best 850 hPa wind climatology (Fig. 2d), while ECHO-G and the SINTEX models fail to produce the extension of the westerlies into the western/central Pacific Ocean (Fig. 2e, f, g). Over the Indian Ocean, the westerlies extend to $\sim 50^\circ\text{E}$. In the ECHAM4/AMIP II run (Fig. 2b), the westerlies over the Indian Ocean are very weak, consistent with the weak convection. With the standard physics, the ECHAM4/HadISST run exhibits an improved climatology (Fig. 2c), but the westerlies are too weak in the central/eastern Indian Ocean in agreement with the location of the convective maximum (Fig. 1c). All of the models are too zonal over the equatorial eastern Indian Ocean near 90°E .

Consistent with observations, the simulated daily variance of OLR is largest where the convection is strongest (not shown). In ECHAM4/AMIP II, the daily variance is overestimated, but this improves in ECHAM4/OPYC and in the SINTEX models. ECHAM4/ HadISST and the ECHO-G models are relatively more consistent in their representation of the variance. In Fig. 3, we show the 20–100 day variance expressed as a percentage of the total daily variance. In observations (Fig. 3a), the intraseasonal signal is strongest in the central/eastern Indian Ocean and the western/central Pacific. ECHAM4/HadISST and ECHO-G best represent the extension of the signal into the Pacific Ocean (Fig. 3c, e, respectively). Like ECHAM4/OPYC (Fig. 3d) the signal over the Indian Ocean is overestimated in ECHO-G (Fig. 3e). The signal is weaker in the SINTEX runs, with the suggestion of off-equatorial maxima (Fig. 3f, g).

3.2 MJO: convection

Sperber (2003) showed the two leading empirical orthogonal functions (EOF's) of MJO convection based on seven winters of 20–100-day-filtered AVHRR OLR. These seven winters (November–March) were characterized as having strong MJO variability. For positive loadings of the principal components (PCs), EOF-1 represents enhanced convection near the Maritime Continent, with suppressed convection over the western/ central Indian Ocean and east of the dateline. EOF-2 is in quadrature with EOF-1 representing enhanced (sup- pressed) convection over the Indian Ocean (western/ central Pacific). Here, we project 20–100-day-filtered AVHRR OLR for the 16 winters of 1979/1980–1994/ 1995, which comprise the AMIPII period, onto the two modes from Sperber (2003, his Fig. 3f, g). The resulting PCs display a characteristic lead–lag relationship, with eastward propagation dominating during each winter (Fig. 4a). Averaged over all winters, PC-2 leads PC-1 by 12 days with a maximum positive correlation of 0.67 (also see Table 2).

In order to perform a consistent analysis across all models, their filtered OLR is projected onto the observed EOF's. This methodology addresses a very specific question: how well do the models represent the observed space–time structure of the MJO? The resulting PCs are examined to identify those years during which their lead–lag relationship is consistent with observations. It is routine to preselect eastward propagating intraseasonal events to best emphasize a model's ability to represent the MJO. For example, Woolnough et al. (2000), Inness and Slingo (2003), and Inness et al. (2003) select individual events by checking that the

convection to the east and west of a base point occurs within predefined lead and lag times. Alternatively, Hendon (2000) filters to isolate eastward zonal wave numbers 1–3 with periods of 35–90 days. In Fig. 4b, the lead–lag relationships of the PCs from ECHO-G are shown. Figure 4c shows the maximum positive correlation as a function of time lag for the individual winters. On the basis of the AVHRR OLR results (the black dots), the observed phase-space occupies the upper right quadrant with the maximum positive correlation being (approximately) greater than or equal to 0.4 for time lags of 5 days or longer. For ECHO-G, we note that 16/19 years-analyzed observations have a maximum positive correlation in the observed phase-space (the red dots; also see Table 2). The average lead–lag relationship for these 16 winters has a more realistic shape and amplitude when compared to that for all 19 winters (Fig. 4b, the dashed black line versus the solid black line), and indicates that the selection process has resulted in more coherent eastward propagation. In the following analysis, we only retain the PCs for those winters during which the maximum positive correlation fell into the observed phase-space. These PCs are used for lagged linear regression to evaluate the space–time structure of the MJO in models and observations.

The observed lag 0 regressions of PCs 1–2 with 20- to 100-day-filtered OLR and 850 hPa wind are shown in Fig. 5a and c. The regressions have been scaled by a 1 standard deviation perturbation of the respective PCs (Table 2), and as in Sperber et al. (1997) and Sperber (2003), the results are plotted where the regression is significant at the 5% level or better assuming that each pentad is independent. The regressions yield OLR anomalies of approximately $\pm 20 \text{ Wm}^{-2}$, with westerly (easterly) anomalies to the west (east) of the anomalous convection. These spatial patterns are consistent with numerous other researchers (e.g., Weickmann et al. 1985; Slingo et al. 1999). The lag 0 regressions using the ECHO-G PCs are given in Fig. 5b and d. The observed quadrature relationship is well represented by the model, though the anomalies are larger than observed, consistent with the inflated standard deviations of its PCs compared to observations (Table 2). All of the EC- HAM4 uncoupled and coupled models have similar spatial patterns compared to ECHO-G (not shown). Like ECHO-G, ECHAM4/OPYC tends to overestimate the magnitude of the OLR anomalies compared to the AVHRR data, though this is less apparent for the remaining models, consistent with their smaller standard deviations in Table 2. For the PC-2 regression, all of the models tend to have a more symmetric response of the suppressed convection over the western Pacific compared to the AVHRR data, where the signal is stronger in the Southern Hemisphere.

Table 2 indicates that the ECHAM4/HadISST, ECHAM4/OPYC, and ECHO-G maximum positive correlations are consistent with observations, while those for ECHAM4/AMIP II and the SINTEX models are weaker than observed. This indicates that the former models have more coherent eastward propagation of OLR anomalies from the Indian Ocean into the western/central Pacific Ocean. All of the models represent well the time lag of the transition of the convective maxima from the Indian Ocean to the western Pacific (Table 2). These results are confirmed in Fig. 6 in which the lag regression of PC-1 with 5°N – 5°S averaged 20–100-day-

filtered OLR are presented. Preceding and following the enhanced convection are periods of suppressed convection that also propagate eastward over the eastern hemisphere. The suppressed phase is best represented in ECHAM4/HadISST, ECHAM4/OPYC, and ECHO-G.

Rainfall anomalies also exhibit eastward propagation, though in the models they are about 0.5 mm day⁻¹ weaker than the CMAP estimates, with the extension into the central Pacific Ocean not as coherent as for the OLR signal (not shown). Over the western Pacific, the simulated rainfall anomalies peak a couple of days in advance of the OLR minima (not shown). Compared to SINTEX-b, SINTEX-a has a better representation of the eastward propagation of convection from the Indian Ocean into the western Pacific (Fig. 6f versus g; Table 2). For the sake of brevity, and due to the lack of comprehensive model output, figures for the ECHAM4/AMIP II and SINTEX-a will not be included in the subsequent analysis.

The SINTEX runs differed in their initial conditions, indicating sensitivity of the MJO convective propagation to the time segment analyzed. In the case of ECHAM4/OPYC and ECHO-G, the time segment analyzed corresponded to the last 20 years (19 winters) of data submitted to PCMDI. However, for these models, approximately 100 years of daily data was available. Compared to the full record, the initial 19-winter-segment-analyzed had a larger maximum positive correlation, though the day at which the maximum positive correlation occurred was robust (Table 2). To test whether such differences are statistically significant, we performed Monte Carlo sampling by randomly selecting the PCs of 19 individual winters from the full dataset and we recalculated the metrics in Table 2. This resampling was performed 500,000 times, resulting in the frequency distributions in Fig. 7. For both ECHAM4/OPYC and ECHO-G, the original estimate of each of the metrics in Table 2 using the last 19 winters of data are within about 1 SD of the Monte Carlo estimates. Thus, the initial 19-year sample from each of these two models gives robust estimates of the Table 2 metrics, assuming that the frequency distributions generated from the Monte Carlo sampling are representative of the true probability distributions.

Figure 7 also indicates that statistically significant differences between ECHAM4/OPYC and ECHO-G exist. Two-tailed *t* tests indicate that the means of the distributions from ECHAM4/OPYC are different from those of ECHO-G at the 1% significance level. We do not have enough data to estimate the frequency distributions of the other models, but the large differences in the means of the maximum positive correlations between the SINTEX and ECHAM4/AMIP II simulations compared to the ECHAM4/OPYC, ECHO-G and ECHAM4/HadISST runs suggests that the eastward propagation of convection between these two groups of models is statistically different (Table 2, Fig. 6). In the case of the coupled models, this suggests that there is sensitivity to the ocean model to which the AGCM is coupled, indicating that different air-sea feedbacks contribute to differences in the coherence of the eastward propagation of convection. This in turn could be related to differences in the mean-state that might arise due to the decision of whether or not to employ flux adjustment. Whether or not the

differences in the east-ward propagation of OLR translate into different operative mechanisms for MJO propagation will be explored shortly.

The Monte Carlo sampling also indicates that the standard deviations of the ECHO-G metrics can be upwards of 50% larger than those for ECHAM4/OPYC (Table 2). This was a surprising result given that the atmospheric models were the same, except for horizontal resolution. Figure 8 shows the mean and the 5% significance levels of the maximum positive correlation between PC-1 and PC-2 for these two models based on Monte Carlo sampling using different numbers of winters. With its larger standard deviation, ECHO-G requires a larger sample size to achieve the same significance level as ECHAM4/OPYC. The implication of the different standard deviations is especially important for evaluating climate-change integrations to investigate anthropogenically forced changes in MJO variability. With the larger standard deviation in ECHO-G, the perturbation in a climate-change run would have to be larger to achieve the same level of significance for a given sample size compared to ECHAM4/OPYC.

3.3 MJO: convection and near-surface fields

Among others, Woolnough et al. (2000) and Sperber (2003) presented well-defined eastward propagating MJO signals in a multitude of near-surface fields and described their phasing relative to the convective maximum. Figure 9 shows the SST and ground temperature anomalies relative to the convection. Prior (after) the maximum enhanced convection, the SST anomalies are above (below) normal. Compared to the observations in Fig. 9a, the coupled models simulate the observed lead-lag SST response, though the simulated SST anomalies at and east of the dateline tend to be too weak (Fig. 9c-e). In the ECHAM4/HadISST run forced with observed monthly SST, a coherent SST signal is absent. Over East Africa ($\sim 35^{\circ}\text{E}$), all of the models qualitatively capture the ground temperature anomalies, though over South America ($\sim 70^{\circ}\text{W}$) only ECHAM4/HadISST and ECHAM4/OPYC capture the proper phasing. As seen in Fig. 10, the eastern hemisphere SST signal is slightly preceded by near-surface zonal wind anomalies, with easterly (westerly) wind anomalies leading the warming (cooling) by about a pentad. In ECHAM4/HadISST and SINTEX-b, Fig. 10b, e, the central Pacific Ocean westerly anomalies are weaker than reanalysis (Fig. 10a). In ECHAM4/OPYC and ECHO-G, Fig. 10c, d, the zonal wind anomalies are stronger than reanalysis, consistent with their overly strong convective anomalies. The wind anomalies influence the surface evaporation (e.g., Shinoda et al. 1999; Sperber 2003), though other factors such as the absolute SST and the vertical gradient of moisture are also important. In the reanalysis over the Indian Ocean, Fig. 11a, the evaporative cooling lags the westerly wind anomalies, while over the western Pacific the lag is not as substantial. While all of the models at least produce eastward propagation of zonal wind anomalies to the western Pacific (Fig. 10b-e), only the ECHAM4/OPYC model captures eastward propagation of latent heat flux anomalies using 5°N - 5°S data (Fig. 11c), though the simulated latent heat flux and zonal wind anomalies are more closely in phase than in the reanalysis. The eastward propagation of the latent heat flux anomalies suggests that the air-sea interaction in ECHAM4/OPYC is more realistic than in the other models. This may be due to

the choice of ocean model, or it may be related to the horizontal resolution of the atmospheric model. ECHAM4/OPYC was run at T42, while the other coupled integrations were run at T30. This suggests that the higher horizontal resolution atmospheric model may be needed to resolve the strong meridional gradient of the near-equatorial zonal wind over the Indian Ocean in order to represent the zonal wind/latent heat flux anomalies seen in the reanalysis. As seen in Fig. 2, poleward of 2.5°N and 10°S, the westerlies transition rapidly into easterlies, and this is best captured in ECHAM4/OPYC.

Important for the SST anomalies are the net surface heat flux anomalies. All of the models exhibit eastward propagation of their intraseasonal net surface heat flux anomalies (e.g., SINTEX-b, Fig. 11f), with the intra-seasonal net surface shortwave radiation being the dominant term (not shown). The influence of the net surface shortwave radiation anomalies in the ECHO-G and the SINTEX models is fortuitous in that it compensates for the incorrect representation of the latent heat flux, thus driving the eastward propagation of the SST anomalies (Fig. 9d–e).

In advance of the deep convection, the build-up of low-level moisture convergence is believed to play a central role in maintaining the eastward propagation of the MJO (e.g. Hendon and Salby 1994; Jones and Weare 1996; Maloney and Hartmann 1998; Sperber 2003). As seen in Fig. 12, the circumnavigating 1000 hPa moisture signal is best represented in ECHAM4/OPYC (Fig. 12c), while the eastern hemispheric signal is captured by ECHO-G (Fig. 12d) and to a lesser extent in SINTEX-b (Fig. 12e). Even in the uncoupled model, ECHAM4/HadISST, eastward propagation is apparent, especially that associated with the suppressed convection over the western/central Pacific Ocean. Similarly, the convergence anomalies that lead the convection are most readily captured by ECHAM4/OPYC and ECHO-G (Fig. 13c, d), while that in the SINTEX runs and the ECHAM4/HadISST simulation are not as coherent as observed (Fig. 13a).

3.4 MJO: vertical structure

Sperber (2003) found a westward vertical tilt of divergence and moisture using the reanalysis. The tilt of the divergence (specific humidity), is seen in Fig. 14 (Fig. 15). These figures are for time lag 0, when the strongest convection is located near 125°E. In this portrayal, the ECHAM4/HadISST, ECHAM4/OPYC, and ECHO-G models are realistic in their representation of the near-surface convergence and moisture build-up that occurs east of the strongest convection, while the SINTEX model produces a more vertically stacked signal. All models tend to produce a mid-tropospheric maxima in the convergence and moisture anomalies, though the level at which the maxima occurs tends to be higher than in the reanalysis, especially for the moisture. Sperber (2003) noted that free-tropospheric interactions were important in the life cycle of the MJO. To the west of the strongest convection, divergence and negative moisture anomalies erode the trailing edge of the convective envelope.

An additional way to examine the vertical structure is to plot lag regressions as a function of pressure level over the western Pacific Ocean (Figs. 16, 17). In reanalysis and the ECHAM4/OPYC and the ECHO-G models, this highlights that the development of convergence and enhanced moisture anomalies occurs first near the surface in advance of the deep convection (Figs. 16a, c, d, 17a, c, d). Despite the lack of a well-pronounced westward vertical tilt in the divergence and moisture in SINTEX-b (Figs. 14e, 15e), the results in Figs. 16e and 17e indicate that enhanced moisture anomalies, and to a lesser extent convergence anomalies, precede the deep convection. In the uncoupled model, ECHAM4/Had- ISST, the divergence and moisture signals do not exhibit a statistically significant signal near the surface.

Overall our results indicate that the coupled models that were flux-adjusted to maintain a basic state close to observed conditions (ECHAM4/OPYC and ECHO-G) best represent the vertical structure of the MJO. SINTEX-b, which was not flux-adjusted, has a less realistic vertical structure, as does ECHAM4/HadISST in which air–sea interaction is not present.

4 Summary and discussion

The MJO is analyzed in ECHAM4 in five different configurations consisting of two runs with different atmospheric physics options forced with prescribed SST, and in three simulations using different ocean models. By projecting the 20–100-day bandpass-filtered OLR from each of the models onto the two leading EOFs derived from AVHRR OLR, our analysis allows direct comparison between each of the models, and with observations. This enables us to make a one-to-one comparison of quantitative metrics for assessing the ability of the models to simulate MJO convection. These metrics include (1) the standard deviations of the PC time series, which are directly proportional to the amplitude of the convective anomalies, (2) the maximum positive correlation between the PC time series, which indicates how coherent the propagation is from the Indian Ocean into the western Pacific, (3) the time lag at which the maximum positive correlation occurs gives the time scale for the transition of convection between the dominant centers of action, and (4) the fraction of years when the eastward propagation is consistent with observations. In the case of ECHAM4/OPYC and ECHO-G, where we have a longer record, we have been able to demonstrate that statistically significant differences in these metrics occur, which indicates that the MJO simulation is sensitive to the ocean model to which ECHAM4 is coupled. The ability to assess significant differences also has implications for comparing MJO in present-day simulations with climate-change runs.

The MJO is simulated well by the ECHAM4 AGCM with standard physics when it is coupled to the OPYC and HOPE-G ocean models in which flux adjustment of heat and freshwater helps maintain a basic state close to present-day conditions. In the SINTEX model, ECHAM4 coupled to the OPA8.1 ocean model, no flux adjustment is employed, and the model has systematically colder SST over much of the Indian Ocean and the equatorial west Pacific. In

conjunction with an SST cold bias, the organization of low-level moisture and convergence anomalies and their phasing with respect to the MJO convective anomalies are less well simulated. On the basis of the afore-mentioned metrics, the SINTEX model does not simulate MJO convection that is as organized as in ECHAM4/OPYC and ECHO-G, or in the AGCM simulation forced with the HadISST. This indicates that in the coupled models, a realistic basic state is at least as important as air–sea interaction. It is possible that if flux adjustment were used in the SINTEX model, its simulation of the MJO would improve. The vertical structure of the simulated MJO has been compared with reanalysis. The flux-adjusted models are more realistic than the SINTEX or the ECHAM4/ HadISST simulations in capturing the near-surface convergence and moisture anomalies that lead the convection. Only the ECHAM4/OPYC model simulates the eastward propagation of enhanced latent heat flux that trails the enhanced convection. Despite this, all of the coupled models generate eastward propagating warming (cooling) of the SST that leads (lags) the MJO convection. This is because the simulated net surface shortwave radiation anomalies dominate the net surface heat flux, unlike reanalysis (Sperber 2003) and estimates during the TOGA-COARE period (Shinoda et al. 1999). This suggests details of the radiative transfer, cloud, and the boundary layer schemes may need to be re-examined in order to properly represent the energy partitioning at the surface for the MJO. Additionally, in the ECHAM4/ OPYC run, the AGCM was run at T42 as compared to T30 for the other coupled runs. A strong meridional gradient in the zonal wind is present over the Indian Ocean, and one possibility is that higher horizontal resolution may be needed to get the realistic latent heat flux propagation. However, to test this conclusively would require two additional simulations: ECHAM4/ OPYC with the AGCM at T30; and ECHO-G with the AGCM at T42. Flux adjustment would be required so that the models have basic states similar to those analyzed herein. However, since ECHAM4 has been superseded by ECHAM5, resources to make these sensitivity tests are not forthcoming.

Contrary to the results of Liess et al. (2004) and Liess and Bengtsson (2004), our results indicate that the ECHAM4/OPYC model gives an excellent representation of the MJO, with improvement associated with air–sea interaction. There are several reasons that may account for this dilemma: (1) while they use the term intraseasonal oscillation (ISO) interchangeably with MJO, their technique for constructing the life cycle of the MJO considered the tropics as whole. Inclusion of other components of intraseasonal variability, such as an overly strong signal near South America (Liess et al. 2004) might contaminate extraction of the MJO signal over the eastern hemisphere. Our MJO results are derived from a more regional analysis and we use a selection criterion for analyzing those winters when the OLR lag correlation and time scale metrics are consistent with observations; (2) their results are based on all seasons, while we have only considered the boreal winter. The MJO also exists during the boreal summer, albeit weaker than during winter, and the northward propagation of convection that accompanies the eastward propagating MJO is an additional level of detail to be represented (and studied); and (3) our results derive from an examination of OLR, as opposed to 200 hPa velocity potential in their work.

The coupled climate simulations presented herein give the best representation of the MJO among its generation of climate models (Sperber et al. 2004b). This is especially true for the models whose basic state is close to observations. The vertical structure of the MJO and the low-level moisture convergence that has been implicated in maintaining the life cycle of the MJO are well represented. Though some problems exist with respect to the surface fluxes, these simulations are benchmarks that indicate state-of-the-art climate models can represent many important aspects of the MJO. This indicates that it is not necessary to embed 2-D cloud resolving models at each GCM gridpoint to obtain a credible simulation of the MJO (Randall et al. 2003).

Acknowledgements K. R. Sperber thanks Dr. B. Santer (PCMDI) for helpful discussions regarding Monte Carlo sampling. This work was performed under the auspices of the U.S. Department of Energy Office of Science, Climate Change Prediction Program by University of California Lawrence Livermore National Laboratory under contract No. W-7405-Eng-48.

References

- AchutaRao K, Covey C, Doutriaux C, Fiorino M, Gleckler P, Phillips T, Sperber K, Taylor K (2004) An appraisal of coupled climate model simulations. In: Bader D (ed) UCRL-TR-202550, PCMDI, Lawrence Livermore National Laboratory, Livermore, CA
- Fairall C, Bradley EF, Rogers DP, Edson JB, Young GS (1996) The TOGA COARE bulk flux algorithm. *J Geophys Res* 101:3747–3764
- Ferranti L, Palmer TN, Molteni F, Klinker E (1990) Tropical- extratropical interaction associated with the 30–60 day oscillation and its impact on medium and extended range prediction. *J Atmos Sci* 47:2177–2199
- Flatau M, Flatau PJ, Phoebus P, Niiler PP (1997) The feedback between equatorial convection and local radiative and evaporative processes: the implication for intraseasonal oscillations. *J Atmos Sci* 54:2373–2386
- Gualdi S, Navarra A (1998) A study of the seasonal variability of the tropical intraseasonal oscillation. *Global Atmos Ocean Syst* 6:337–372
- Gualdi S, Navarra A, von Storch H (1997) Tropical intraseasonal oscillation appearing in operational analyses and in a family of general circulation models. *J Atmos Sci* 54:1185–1202
- Gualdi S, Navarra A, Tinarelli G (1999) The interannual variability of the Madden–Julian oscillation in an ensemble of GCM simulations. *Clim Dynam* 15:643–658
- Gualdi S, Guilyardi E, Navarra A, Masina S, Delecluse P (2003) The interannual variability in the tropical Indian Ocean as simulated by a CGCM. *Clim Dynam* 20:567–582. DOI 10.1007/s00382-002-0295-z

- Guilyardi E, Madec G, Terray L (2001) The role of lateral ocean physics in the upper ocean thermal balance of a coupled ocean atmosphere GCM. *Clim Dynam* 17:589–599
- Guilyardi E, Delecluse P, Gualdi S, Navarra A (2003) Mechanisms for ENSO phase change in a coupled GCM. *J Clim* 16:1141– 1158
- Hendon HH (2000) Impact of air–sea coupling on the Madden–Julian oscillation in a general circulation model. *J Atmos Sci* 57:3939–3952
- Hendon HH, Salby ML (1994) The life cycle of the Madden–Julian oscillation. *J Atmos Sci* 51:2225–2237
- Hendon HH, Zhang C, Glick JD (1999) Interannual variation of the Madden–Julian oscillation during Austral summer. *J Clim* 12:2538–2550
- Higgins RW, Schemm J-KE, Shi W, Leetma A (2000) Extreme precipitation events in the western United States related to tropical forcing. *J Clim* 13:793–820
- Inness PM, Slingo JM (2003) Simulation of the Madden–Julian oscillation in a coupled general circulation model. Part I: comparison with observations and an atmosphere-only GCM. *J Clim* 16:345–364
- Inness PM, Slingo JM, Woolnough SJ, Neale RB, Pope VD (2001) Organization of tropical convection in a GCM with varying vertical resolution: implications for the simulation of the Madden–Julian oscillation. *Clim Dynam* 17:777–793
- Inness PM, Slingo JM, Guilyardi E, Cole J (2003) Simulation of the Madden–Julian oscillation in a coupled general circulation model. Part II: the role of the basic state. *J Clim* 16:365–382
- Jones C, Weare BC (1996) The role of low-level moisture convergence and ocean latent heat fluxes in the Madden and Julian oscillation. *J Clim* 9:3086–3140
- Kalnay E, Kanamitsu M, Kistler R, Collins W, Deaven D, Gandin L, Iredell M, Saha S, White G, Woollen J, Zhu Y, Chelliah M, Ebisuzaki W, Higgins W, Janowiak J, Mo KC, Ropelewski C, Wang J, Leetma A, Reynolds R, Jenne R, Joseph D (1996) The NCEP/NCAR 40-year reanalysis project. *Bull Amer Met Soc* 77:437–471
- Kemball-Cook S, Wang B, Fu X (2002) Simulation of the intra- seasonal oscillation in the ECHAM-4 model: the impact of coupling with an ocean model. *J Atmos Sci* 59:1433–1453
- Legutke S, Maier-Reimer E (1999) Climatology of the HOPE-G global ocean general circulation model. Technical Report No. 21, German Climate Computer Centre (DKRZ), Hamburg, Germany, p 90

- Legutke S, Voss R (1999) The Hamburg atmosphere-ocean coupled circulation model ECHO-G. Technical Report No. 18, German Climate Computer Centre (DKRZ), Hamburg, Germany, p 62
- Liess S, Bengtsson L (2004) The intraseasonal oscillation in ECHAM4. Part II: sensitivity studies. *Clim Dynam* 22:671–688. DOI 10.1007/s00382-004-0407-z
- Liess S, Bengtsson L, Arpe K (2004) The intraseasonal oscillation in ECHAM4. Part I: coupled to a comprehensive ocean model. *Clim Dynam* 22:653–669. DOI 10.1007/s00382-004-0406-0
- Madden RA, Julian PR (1971) Detection of a 40–50 day oscillation in the zonal wind in the tropical Pacific. *J Atmos Sci* 28:702–708
- Madden RA, Julian PR (1972) Description of global-scale circulation cells in the tropics with a 40–50 day period. *J Atmos Sci* 29:1109–1123
- Madden RA, Julian PR (1994) Observations of the 40–50 day tropical oscillation—a review. *Mon Weather Rev* 122:814–837
- Madec G, Delecluse P, Imbard M, Levy C (1998) OPA version 8.1 ocean general circulation model reference manuel. Technical Report Note 11, LODYC/IPSL, Paris, France, p 91
- Maloney ED, Hartmann DL (1998) Frictional moisture convergence in a composite life cycle of the Madden–Julian oscillation. *J Clim* 11:2387–2403
- Matthews AJ (2004) Atmospheric response to observed intraseasonal tropical sea surface temperature anomalies. *Geophys Res Lett* 13:L14107. DOI 10.1029/2004GL020474
- McPhaden M (1999) Genesis and the evolution of the 1997–98 El Nino. *Science* 283:950–954
- McPhaden M (2004) Evolution of the 2002/03 El Nino. *Bull Amer Meteorol Soc* 85:677–695
- Min S-K, Legutke S, Hense A, Kwon W-T (2004) Climatology and internal variability in a 1000-year control simulation with the coupled climate model ECHO-G. Technical Report No. 2, Model and Data Group, Max Planck Institute for Meteorology, Hamburg, Germany, p 67
- Mo KC, Higgins RW (1996) Large-scale atmospheric moisture transport as evaluated in the NCEP/NCAR and NASA/DAO reanalyses. *J Clim* 9:1531–1545
- Mo KC, Higgins RW (1998) Tropical influences on California precipitation. *J Clim* 11:412–430
- Murakami T (1988) Intraseasonal atmospheric teleconnection patterns during Northern Hemisphere winter. *J Clim* 1:117–131
- Nordeng TE (1994) Extended versions of the convective parameterizations scheme at ECMWF and their impact on the mean and transient activity of the model in the tropics. ECMWF Tech. Memo. 206, ECMWF, Reading, UK, p 41
- Oberhuber J (1993a) Simulation of the Atlantic circulation with a coupled sea ice-mixed layer-isopycnal general circulation model. Part I: model description. *J Phys Oceanogr* 22:808–829

- Oberhuber J (1993b) The OPYC ocean general circulation model. Tech. Rep. No. 7, Deutsches Klimarechenzentrum GmbH, Hamburg, Germany, p 127
- Pan HL, Wu WS (1994) Implementing a mass-flux convection parameterization package for the NMC medium-range forecast model. In: Proceedings of the 10th conference on numerical weather prediction, Portland/Oregon. American Meteorological Society, pp 96–98
- Randall D, Khairoutdinov M, Arakawa A, Grabowski W (2003) Breaking the cloud parameterization deadlock. *Bull Amer Meteorol Soc* 84:1547–1564
- Rayner NA, Parker DE, Frich P, Horton EB, Folland CK, Alexander LV (2000) SST and sea-ice fields for ERA-40. In: Proceedings of the 2nd WCRP international conference on reanalyses. Reading, August 1999, WCRP-109, WMO/TD-985, pp 18–21
- Reynolds RW, Smith TM (1994) Improved global sea surface temperature analyses using optimum interpolation. *J Clim* 7:929–948
- Roeckner E, Arpe K, Bengtsson L, Christoph M, Claussen M, Dumenil L, Esch M, Giorgetta M, Schlese U, Schulzweida U (1996) The atmospheric general circulation model ECHAM-4: model description and simulation of present-day climate. Rep. No. 218, Max Planck Institute for Meteorology, Hamburg, Germany, p 90
- Shinoda T, Hendon HH (1998) Mixed layer modeling of intra- seasonal variability in the tropical western Pacific and Indian oceans. *J Clim* 11:2668–2684
- Shinoda T, Hendon HH, Glick J (1999) Intraseasonal surface fluxes in the tropical western Pacific and Indian Oceans from NCEP reanalyses. *Mon Weather Rev* 127:678–693
- Slingo JM (1987) The development and verification of a cloud prediction scheme for the ECMWF model. *Q J R Meteorol Soc* 113:899–927
- Slingo JM, Sperber KR, Boyle JS, Ceron J-P, Dix M, Dugas B, Ebisuzaki W, Fyfe J, Gregory D, Gueremy J-F, Hack J, Harzallah A, Inness P, Kitoh A, Lau WK-M, McAvaney B,
- Madden R, Matthews A, Palmer TN, Park C-K, Randall D, Renno N (1996) Intraseasonal oscillations in 15 atmospheric general circulation models: results from an AMIP diagnostic subproject. *Clim Dynam* 12:325–357
- Slingo JM, Rowell DP, Sperber KR, Nortley F (1999) On the predictability of the interannual behaviour of the Madden–Julian oscillation and its relationship with El Nino. *Q J R Meteorol Soc* 125:583–609
- Sperber KR (2003) Propagation and the vertical structure of the Madden–Julian oscillation. *Mon Wea Rev* 131:3018–3037

- Sperber KR (2004a) Madden-Julian variability in NCAR CAM2.0 and CCSM2.0. *Clim Dynam* 23:259–278. DOI 10.1007/s00382-004-0447-4
- Sperber KR (2004b) The Madden–Julian oscillation. Chapter 6.4 in an appraisal of coupled climate model simulations. In: Bader D (ed) UCRL-TR-202550, PCMDI, Lawrence Livermore National Laboratory, Livermore, CA, pp 146–158
- Sperber KR, Slingo JM, Inness PM, Lau WK-M (1997) On the maintenance and initiation of the intraseasonal oscillation in the NCEP/NCAR reanalysis and in the GLA and UKMO AMIP simulations. *Clim Dynam* 13:769–795
- Stendel M, Arpe K (1997) Evaluation of the hydrological cycle in reanalyses and observations. Report No. 228, Max-Planck- Institut für Meteorologie, Hamburg, Germany, p 52
- Stendel M, Roeckner E (1998) Impacts of horizontal resolution in simulated climate statistics in ECHAM4. Max Planck Institute for Meteorology, Rep. No. 253, p 57
- Tiedtke M (1989) A comprehensive mass flux scheme for cumulus parameterization in large-scale model. *Mon Weather Rev* 117:1779–1800
- Tokioka T, Yamazaki K, Kitoh A, Ose T (1988) The equatorial 30–60 day oscillation and the Arakawa–Schubert penetrative cumulus parameterization. *J Meteorol Soc Jpn* 66:883–900
- Valcke S, Terray L, Piacentini A, (2000) The OASIS coupler user guide, Version 2.4. Technical report TR/CMGC/00–10, CERFACS, France, p 77
- Waliser DE, Lau K-M, Kim J-H (1999) The influence of coupled sea surface temperatures on the Madden–Julian oscillation: a model perturbation experiment. *J Atmos Sci* 56:333–358
- Wang WQ, Schlesinger ME (1999) The dependence on convective parameterization of the tropical intraseasonal oscillation simulated by the UIUC 11-layer atmospheric GCM. *J Clim* 12:1423–1457
- Weickmann KM, Lussky GR, Kutzbach JE (1985) Intraseasonal (30–60 day) fluctuations of outgoing longwave radiation and 250 mb streamfunction during northern winter. *Mon Weather Rev* 113:941–961
- Woolnough SJ, Slingo JM, Hoskins BJ (2000) The relationship between convection and sea surface temperature on intraseasonal timescales. *J Clim* 13:2086–2104
- Woolnough SJ, Slingo JM, Hoskins BJ (2001) The organization of tropical convection by intraseasonal sea surface temperature anomalies. *Q J R Meteorol Soc* 127:887–907

Xie P, Arkin P (1997) Global precipitation: a 17-year monthly analysis based on gauge observations, satellite estimates, and numerical model outputs. Bull Amer Meteorol Soc 78:2539– 2558

Table 1 Given are the model designations, the horizontal resolution of the atmospheric model, the prescribed SST or ocean model and the associated horizontal resolution, and notes regarding the experiments

Model designation	AGCM horizontal resolution	SST or OGCM/ horizontal resolution	Notes
ECHAM4/AMIPII	T42	AMIPII SST/T42	AMIPII physics option
ECHAM4/HadISST	T30	HadISST/T30	AGCM: standard physics
ECHAM4/OPYC3	T42	OPYC3/T42 ^a	AGCM: standard physics; flux adjustment of heat and fresh water; 124 years of daily data available
ECHO-G	T30	HOPE-G/T42 ^a	AGCM: standard physics; flux adjustment of heat and fresh water; 100 years of daily data available
SINTEX-a	T30	OPA8.1/2.0°x1.5° ^a	AGCM: standard physics; no flux adjustment;
SINTEX-b			two simulations from different initial conditions

^aEnhanced meridional resolution in the tropics

Table 2 Given are the observed/model data analyzed, the standard deviations of PC-1 and PC-2, the maximum positive correlation, R, between PC-1 and PC-2 and the time lag at which it occurred, and the fraction of years during which the latter two metrics were consistent with observations (see Fig. 4). For EC- HAM4/OPYC and ECHO-G, their first entry is based on the analysis of 19 winters. Their second entries are the metrics based on the full record available (123 and 99 winters, respectively). Their third entries are the metrics based on Monte Carlo sampling 19 winters from the full record, including the ± 1 “standard deviations” of the frequency distributions (Fig. 7). These are used to assess the robustness of the metrics in their first entries. The fourth entry for ECHAM4/OPYC is for Monte Carlo sampling of 19 winters from a pool of 99 winters. This provides a direct comparison to the ECHO-G Monte Carlo sampling metrics

Observations/model	PC-1	PC-2	R	Lag (days) PC-2 leads PC-1 (positive)	No. of years eastward/total
AVHRR	211.3	205.6	0.67	12	16/16
ECHAM4/AMIP II	221.2	232.2	0.43	12	11/16
ECHAM4/HadISST	221.2	179.5	0.64	11	15/16
ECHAM4/OPYC3	245.8	217.9	0.71	11	19/19
ECHAM4/OPYC3 (123 years)	254.8	209.5	0.69	11	115/123
ECHAM4/OPYC3 (19/123 years random)	254.64 \pm 10.85	209.34 \pm 8.09	0.696 \pm 0.029	10.63 \pm 0.55	17.76 \pm 0.99/19
ECHAM4/OPYC3 (19/99 years random)	257.29 \pm 10.88	208.48 \pm 8.32	0.694 \pm 0.029	10.56 \pm 0.56	17.46 \pm 1.07/19
ECHO-G	293.8	267.1	0.68	12	16/19
ECHO-G (99 years)	273.2	250.2	0.63	12	83/99
ECHO-G (19/99 years random)	272.96 \pm 13.10	249.95 \pm 12.08	0.630 \pm 0.046	11.62 \pm 0.68	15.93 \pm 1.45/19
SINTEX-a	240.8	207.6	0.50	12	15/19
SINTEX-b	200.6	199.5	0.43	12	14/19

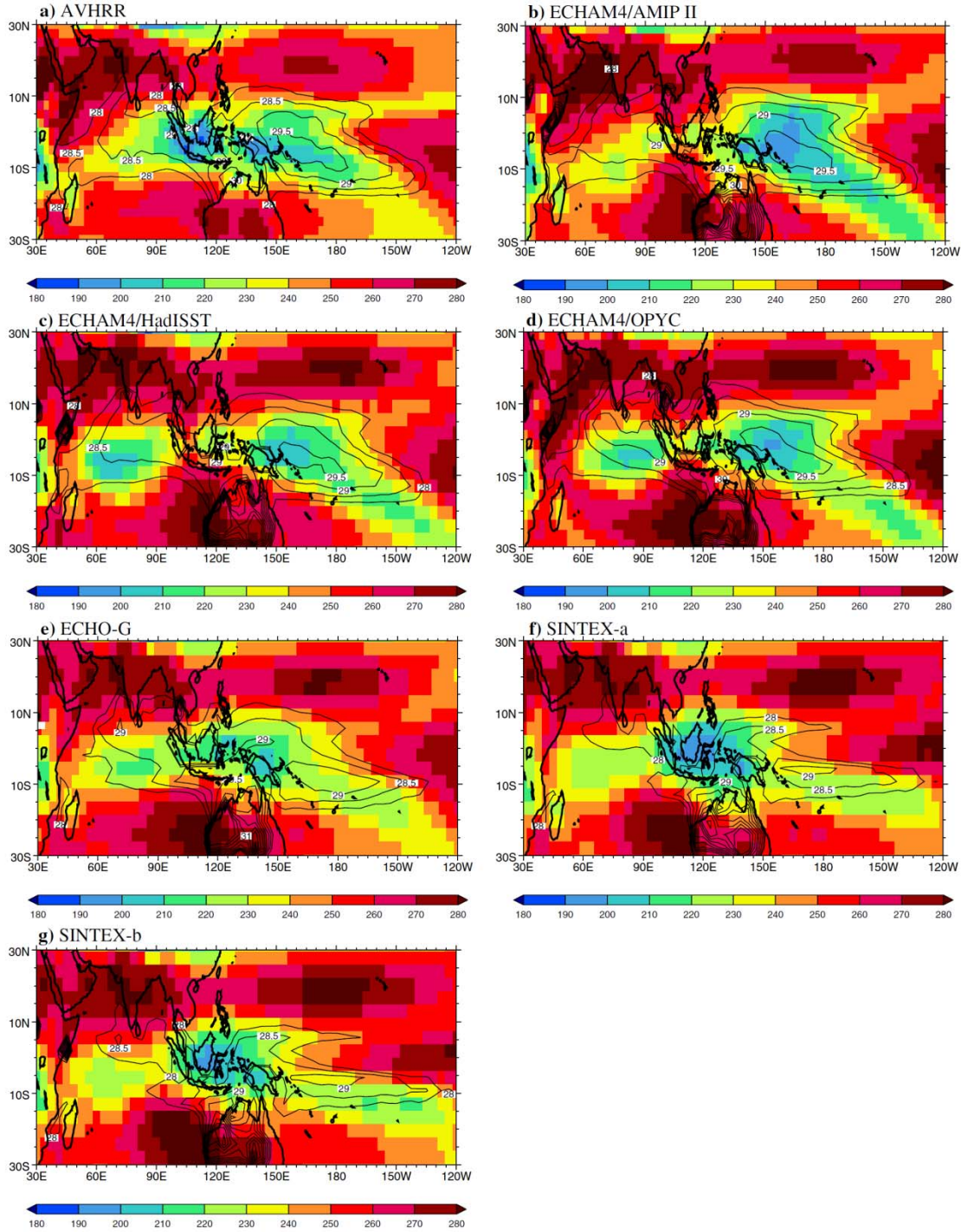


Fig. 1 November–March climatology of outgoing longwave radiation (OLR; W m^{-2}) and SST and ground temperature ($^{\circ}\text{C}$). a AVHRR and HadISST, b ECHAM4/AMIP II, c ECHAM4/HadISST, d ECHAM4/OPYC, e ECHO-G, f SINTEX-a, g SINTEX-b. Isotherms are plotted from 28°C with an increment of 0.5°C

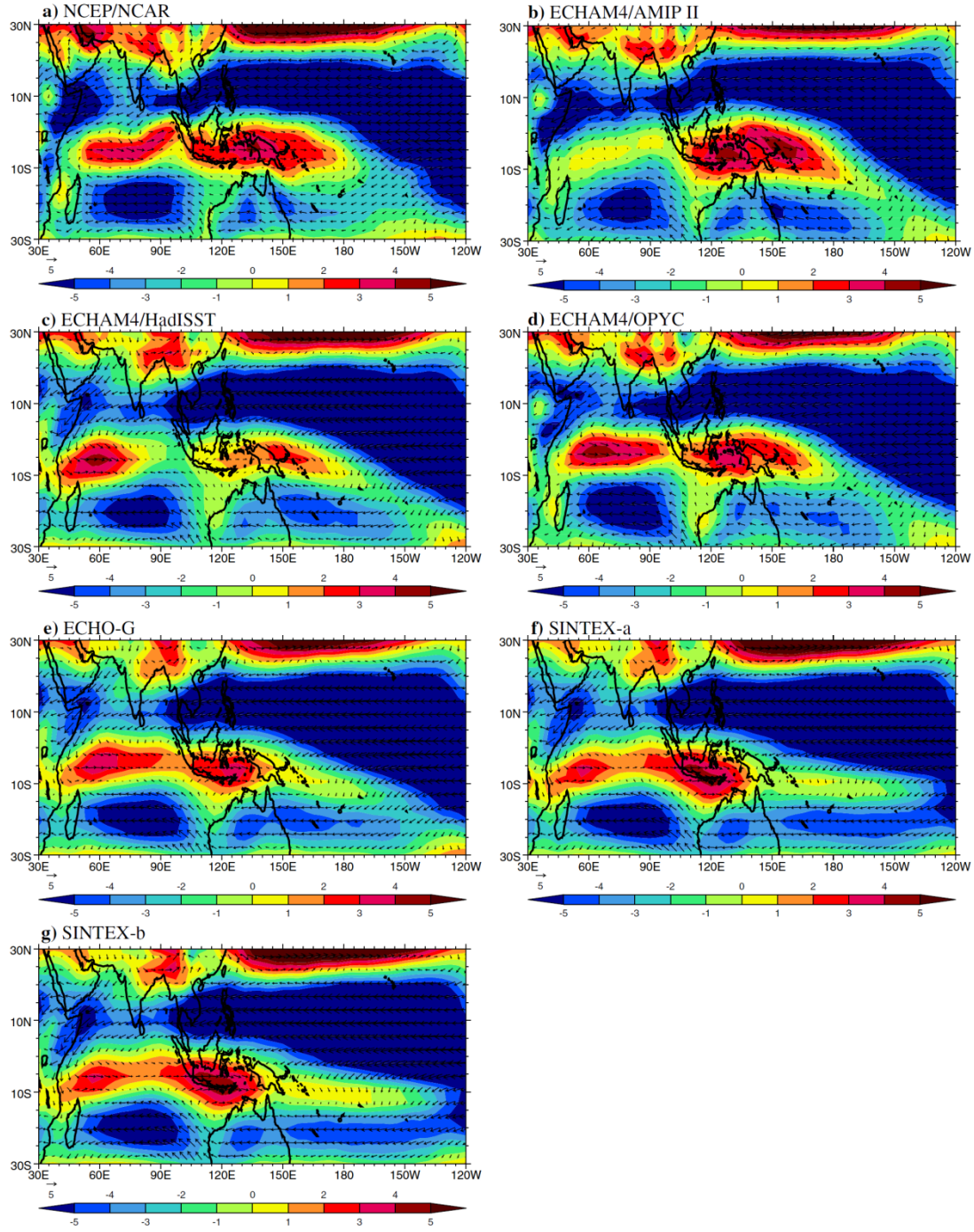


Fig. 2 November–March climatology of 850 hPa wind. a NCEP/ NCAR reanalysis, b ECHAM4/AMIP II, c ECHAM4/HadISST, d ECHAM4/OPYC, e ECHO-G, f SINTEX-a, g SINTEX-b. Every other vector in longitude is plotted for the NCEP/NCAR reanalysis, ECHAM4/AMIP II, and ECHAM4/OPYC. The zonal wind climatology is shaded. A unit vector is 5 m s^{-1}

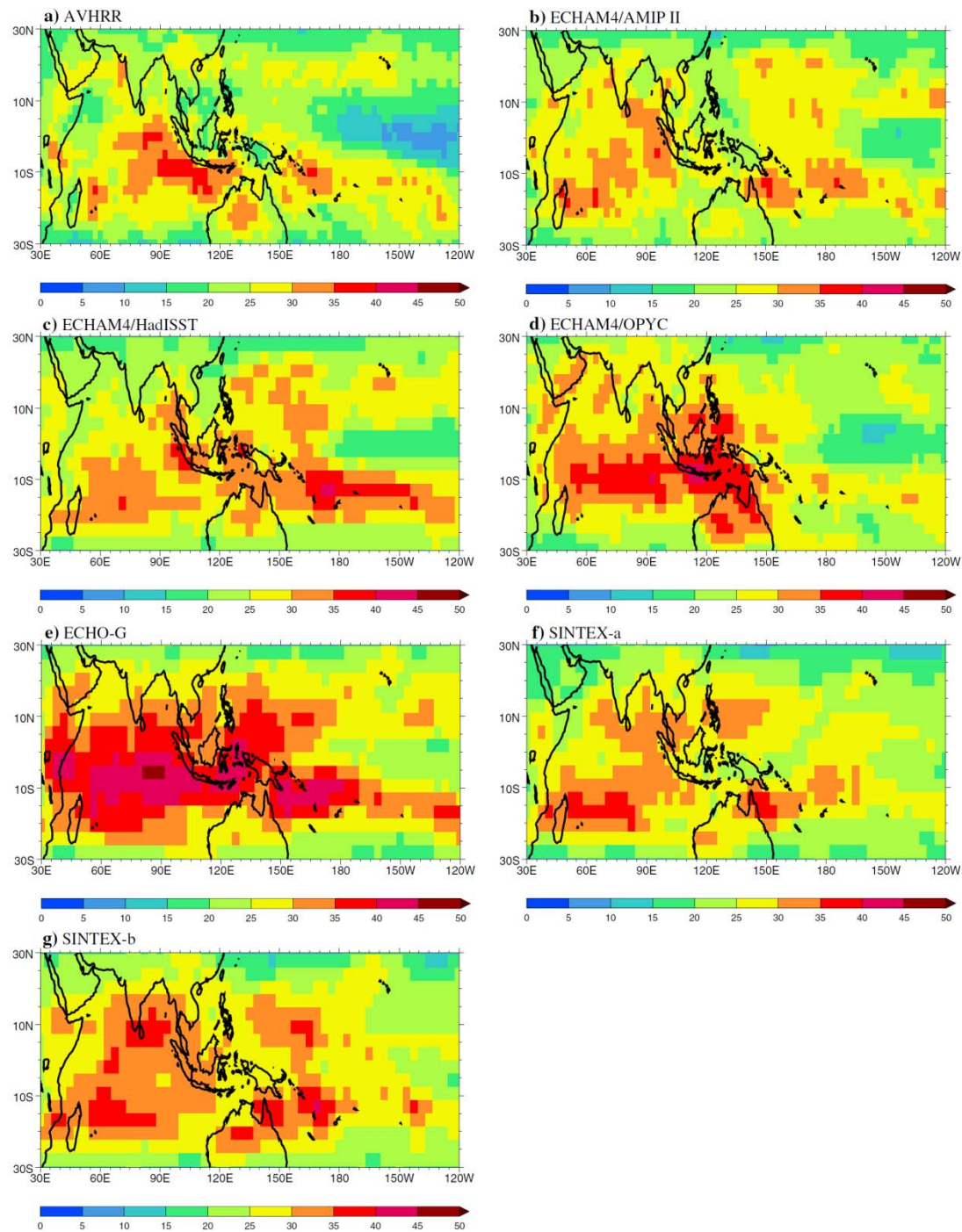


Fig. 3 Percent of daily OLR variance explained by periods of 20–100 days for November–March (%). a AVHRR, b ECHAM4/AMIP II, c ECHAM4/HadISST, d ECHAM4/OPYC, e ECHO-G, f SINTEX-a, g SINTEX-b

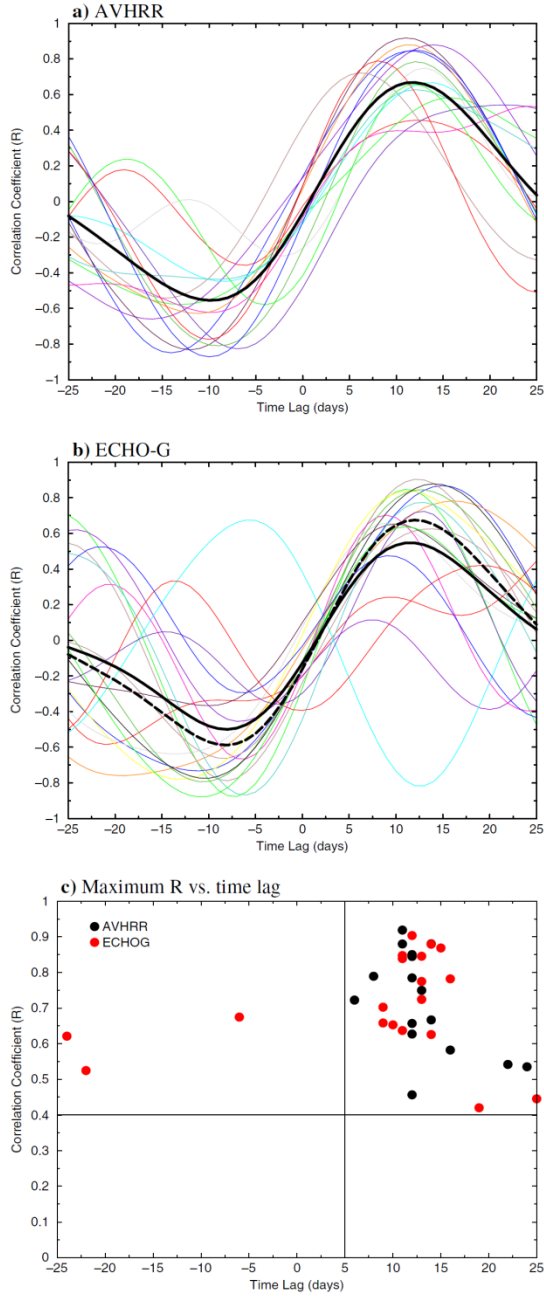


Fig. 4 Lead-lag correlation of PC-1 and PC-2 for each winter. At positive time lags, PC-2 leads PC-1, consistent with eastward propagation of MJO convection. The solid black line is the average lead-lag relationship, and the black dashed line is the average for those winters during which the maximum positive correlation occurred in the observed phase-space in (c). a AVHRR, b ECHO-G. c From the lead-lag relationships for each winter in (a) and (b), the maximum positive correlations are plotted as a function of the time lag at which they occurred. The upper right quadrant, corresponding to the maximum positive correlation being greater than or equal to 0.4 at time lags of 5–25 days, is the observed phase-space in which all of the AVHRR maxima lie

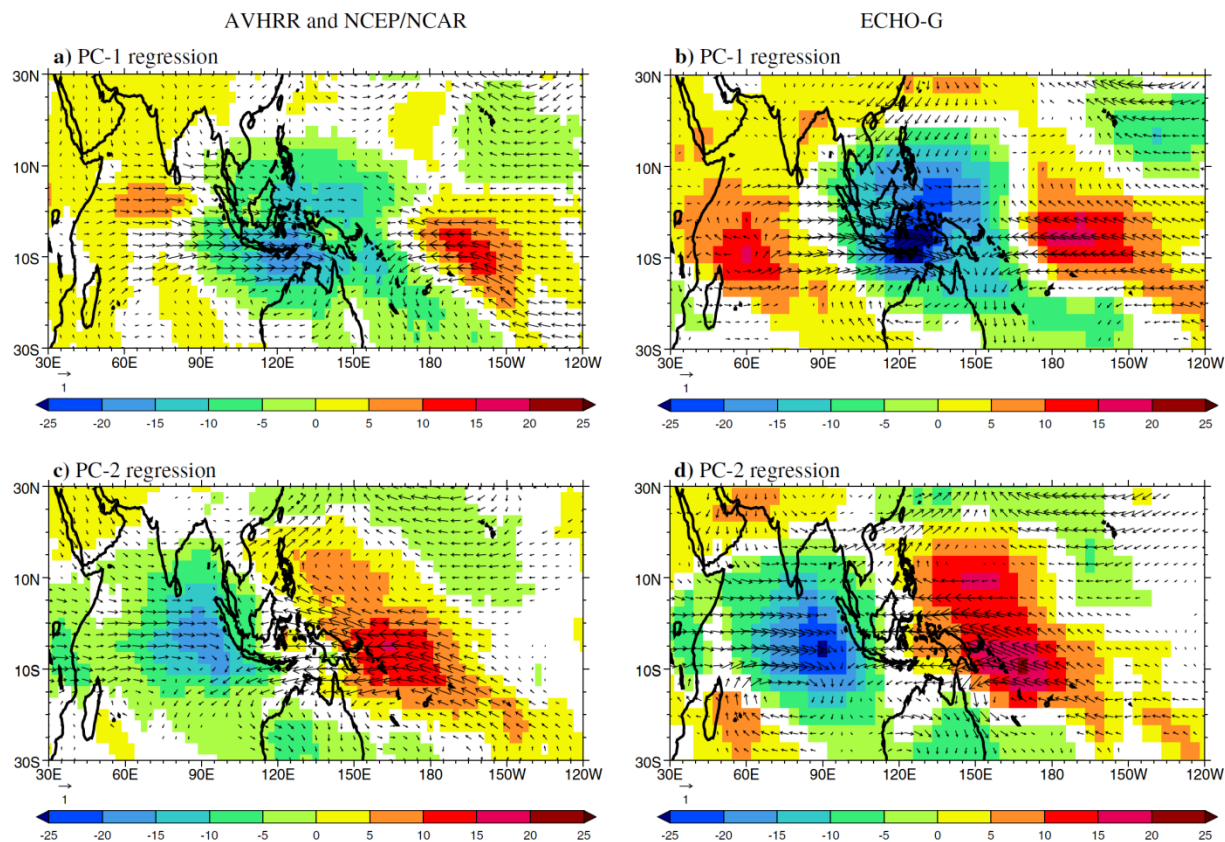


Fig. 5 Lag 0 regression of the principal components (PCs) with 20– 100-day bandpass-filtered OLR and 850 hPa wind. PC-1: a AVHRR OLR and NCEP/NCAR reanalysis, b ECHO-G; PC-2: c AVHRR and NCEP/NCAR reanalysis, d ECHO-G. The regression fits have been scaled by a 1 standard deviation perturbation of the PC's to give units of Wm^{-2} for OLR and m s^{-1} for the wind

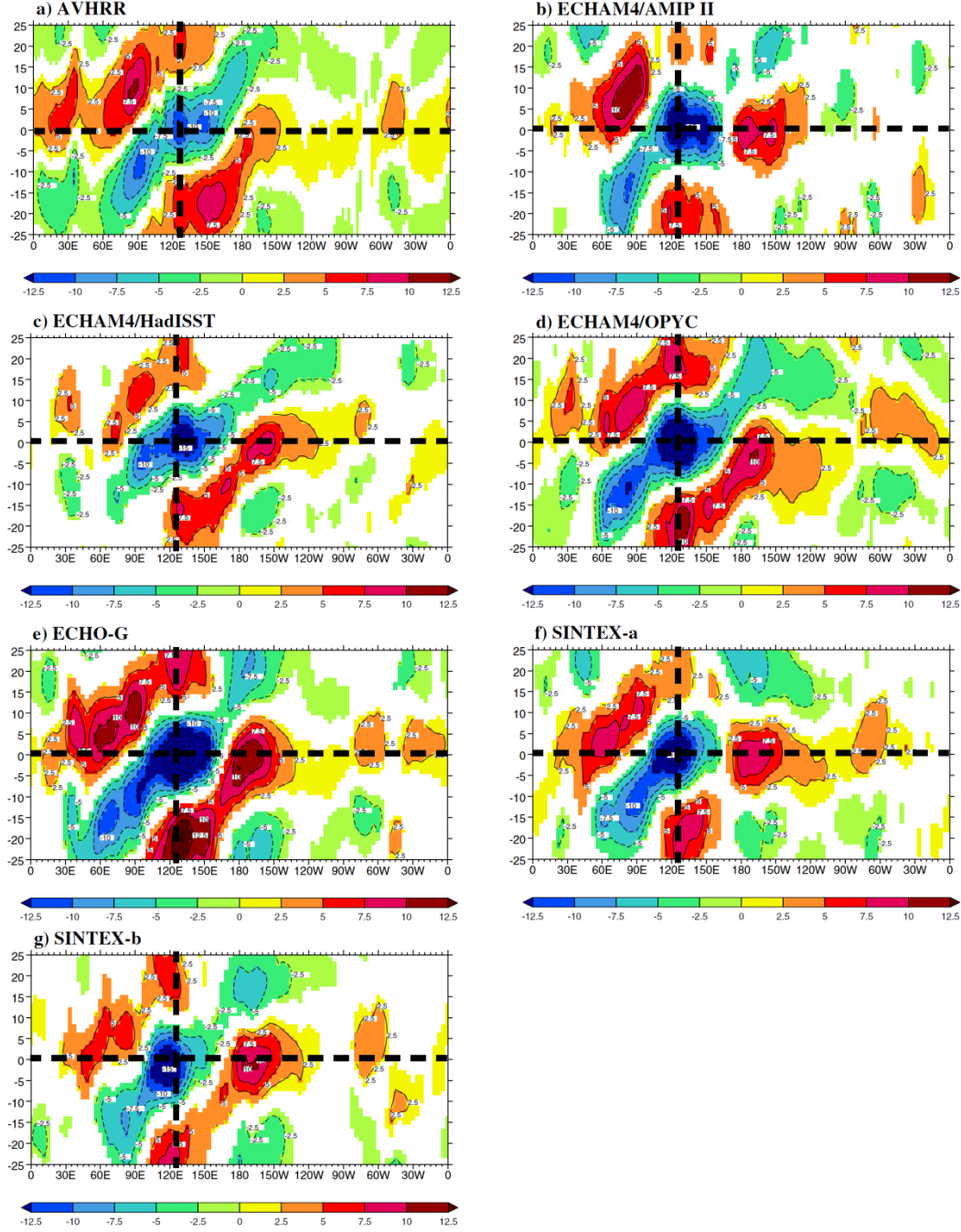


Fig. 6 Lag regression of PC-1 with 5°N–5°S averaged 20–100-day bandpass-filtered OLR. a AVHRR, b ECHAM4/AMIP II, c ECHAM4/HadISST, d ECHAM4/OPYC, e ECHO-G, f SINTEX-a, g SINTEX-b. The regressions have been scaled by a 1 standard deviation perturbation of the respective PCs (Table 2) to give units of Wm^{-2} . Isolines of the OLR anomalies are also plotted at an interval of 2.5 Wm^{-2} . The vertical dashed line is the longitude of maximum convection at lag 0 (given by the horizontal dashed line). On the y-axis, the time lags are from -25 days to 25 days

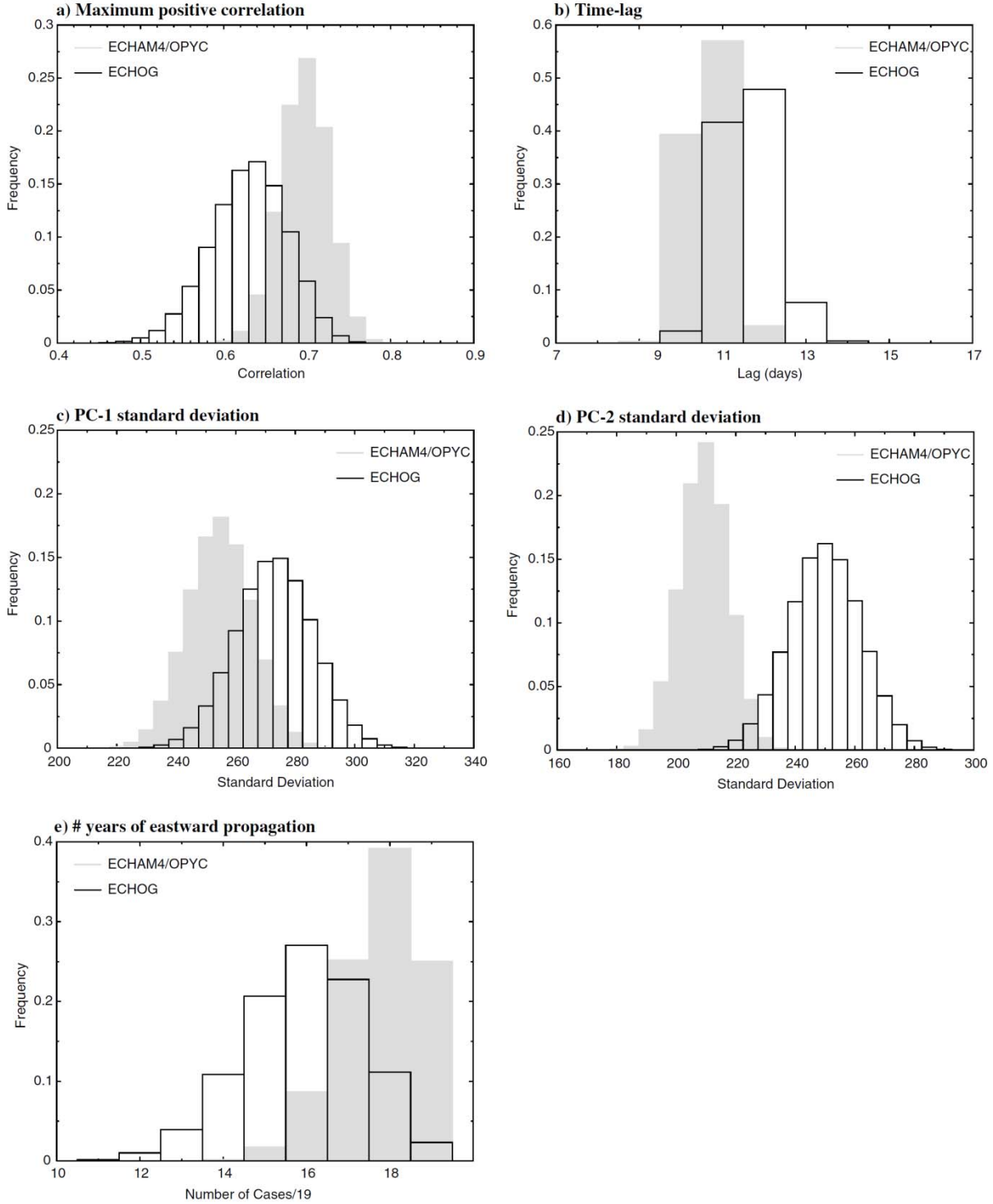


Fig. 7 Frequency distributions of Table 2 metrics for ECHAM4/ OPYC (ECHO-G) based on randomly sampling 19 individual winters of data from the 123 (99) available a maximum positive correlation, b time lag at which the maximum positive correlation occurred, c PC-1 standard deviation, d PC- 2 standard deviation, e number of years with eastward propagation of the 19 sampled. The mean and standard deviations of the distributions are given in Table 2

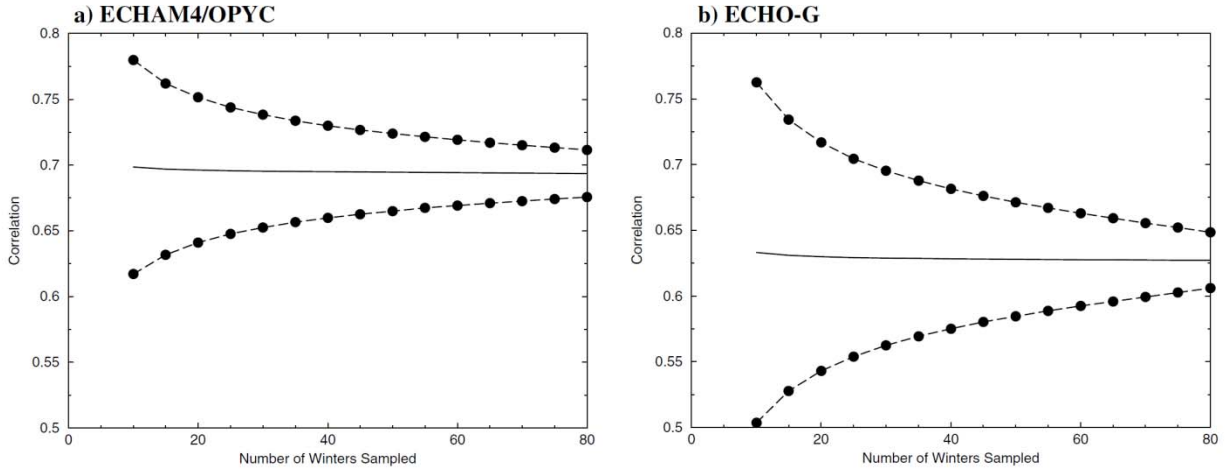


Fig. 8 Mean (solid line) and 5% significance levels (dotted lines) of the average maximum positive correlation based on sampling different number of winters, N . The PCs from N winters were randomly selected 500,000 times to generate frequency distributions of the average maximum positive correlation in order to estimate the 5% significance levels

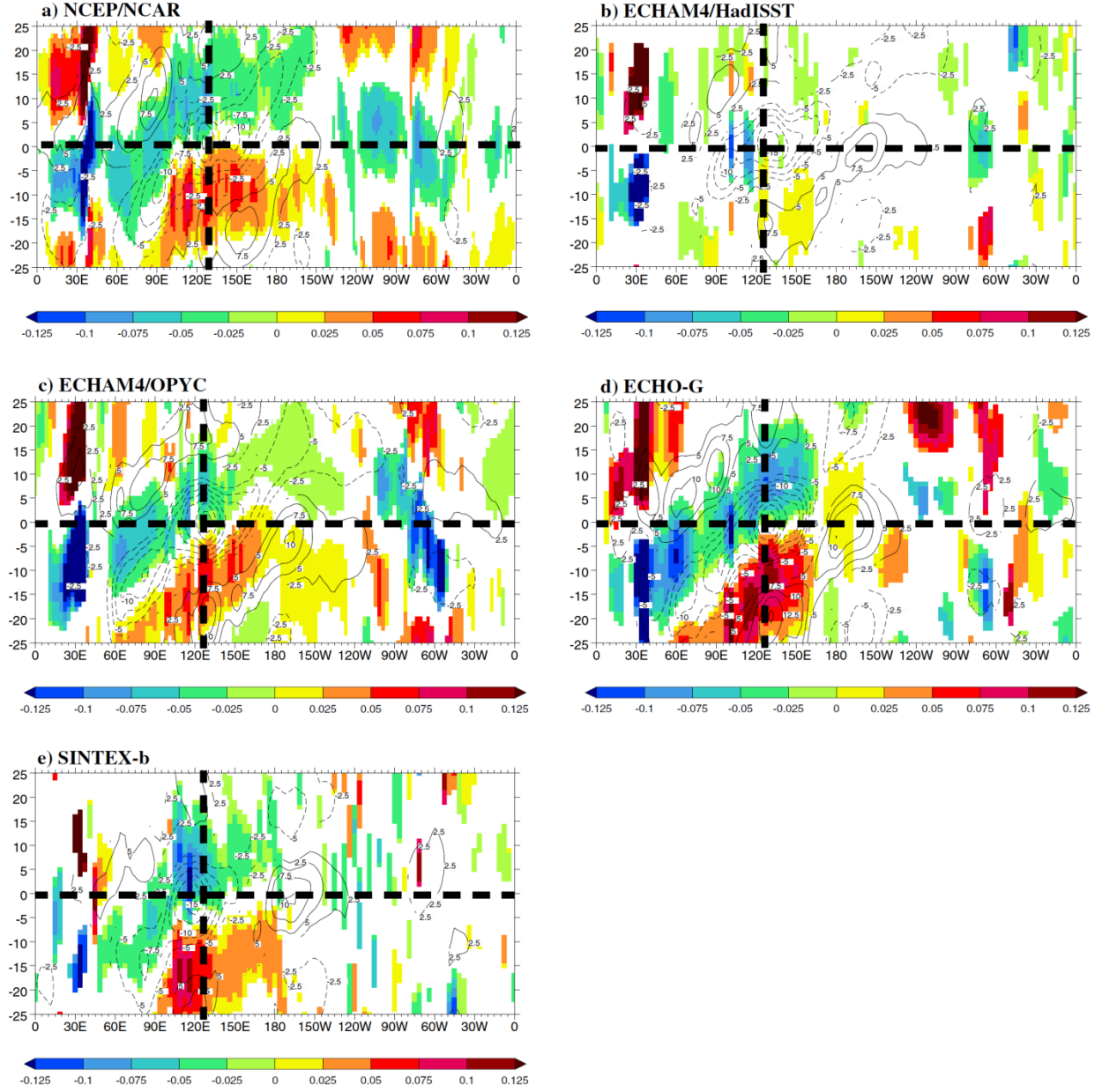


Fig. 9 Lag regression of PC-1 with 5°N–5°S averaged 20–100-day bandpass-filtered sea-surface temperature and ground temperature. a NCEP/NCAR, b ECHAM4/HadISST, c ECHAM4/OPYC, d ECHO-G, e SINTEX-b. The regressions have been scaled by a 1 SD perturbation of the respective PCs (Table 2) to give units of °C. Isolines of the OLR anomalies are also plotted at an interval of 2.5 Wm⁻². The vertical dashed line is the longitude of maximum convection at lag 0 (given by the horizontal dashed line). On the y-axis, the time lags are from -25 days to 25 days

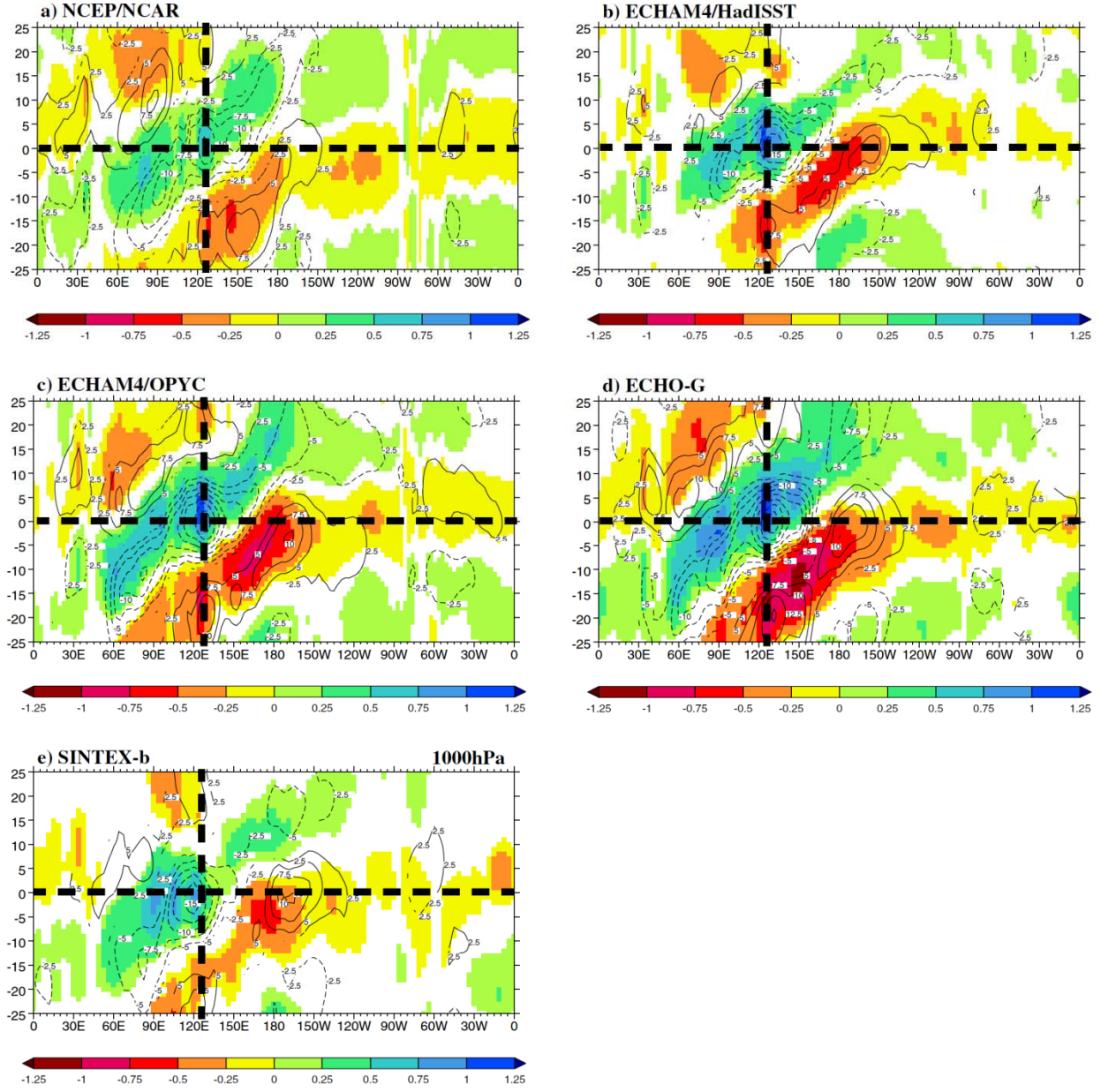


Fig. 10 Lag regression of PC-1 with 5°N–5°S averaged 20–100-day bandpass-filtered surface zonal wind. a NCEP/NCAR, b ECHAM4/HadISST, c ECHAM4/OPYC, d ECHO-G, e SINTEX-b (1000 hPa). The regressions have been scaled by a 1 SD perturbation of the respective PCs (Table 2) to give units of ms^{-1} . Isolines of the OLR anomalies are also plotted at an interval of 2.5 Wm^{-2} . The vertical dashed line is the longitude of maximum convection at lag 0 (given by the horizontal dashed line). On the y-axis, the time lags are from -25 days to 25 days

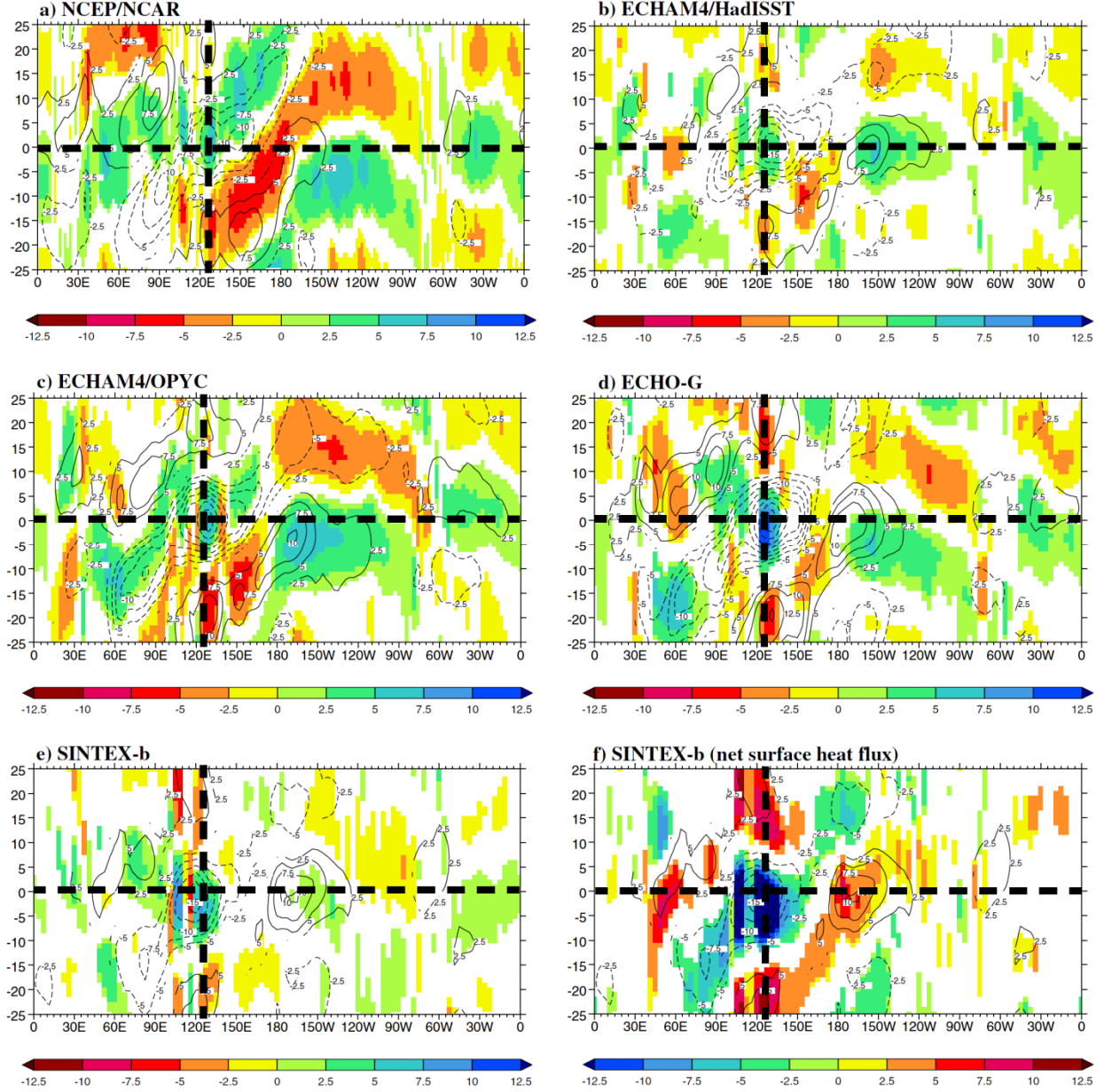


Fig. 11 Lag regression of PC-1 with 5°N–5°S averaged 20–100 day bandpass filtered latent heat flux. a NCEP/NCAR, b ECHAM4/HadISST, c ECHAM4/OPYC, d ECHO-G, e SINTEX-b, f SINTEX-b for net surface heat flux. The regressions have been scaled by 1 SD perturbation of the respective PCs (Table 2) to give units of Wm^{-2} . Positive values indicate evaporative cooling of the surface. Isolines of the OLR anomalies are also plotted at an interval of 2.5 Wm^{-2} . The vertical dashed line is the longitude of maximum convection at lag 0 (given by the horizontal dashed line). On the y-axis, the time lags are from -25 days to 25 days

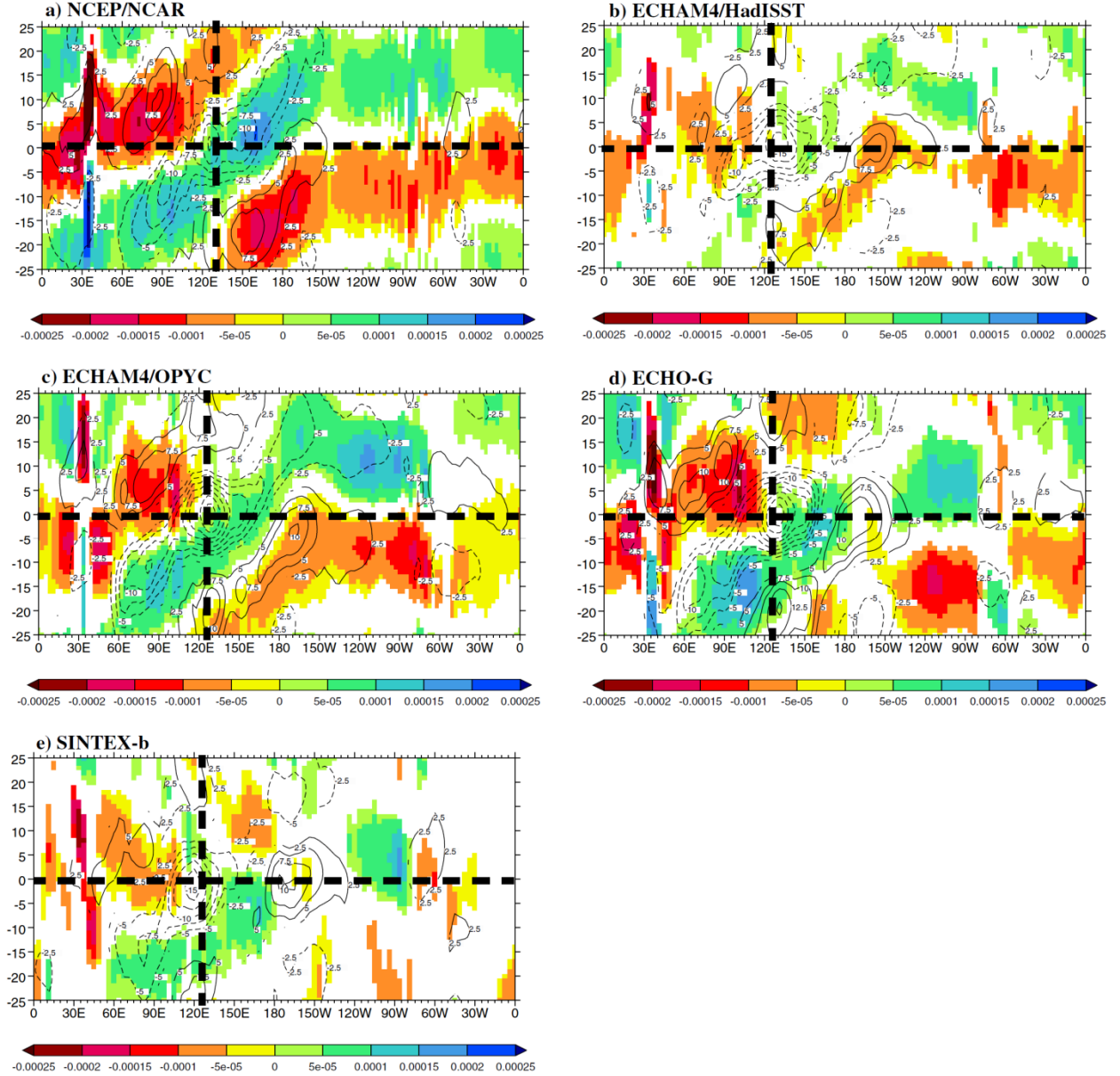


Fig. 12 Lag regression of PC-1 with 5°N–5°S averaged 20–100-day bandpass-filtered 1000 hPa specific humidity. a NCEP/NCAR, b ECHAM4/HadISST, c ECHAM4/OPYC, d ECHO-G, e SINTEX-b. The regressions have been scaled by a 1 SD perturbation of the respective PCs (Table 2) to give units of kg kg^{-1} . Isolines of the OLR anomalies are also plotted at an interval of 2.5 Wm^{-2} . The vertical dashed line is the longitude of maximum convection at lag 0 (given by the horizontal dashed line). On the y-axis, the time lags are from -25 days to 25 days

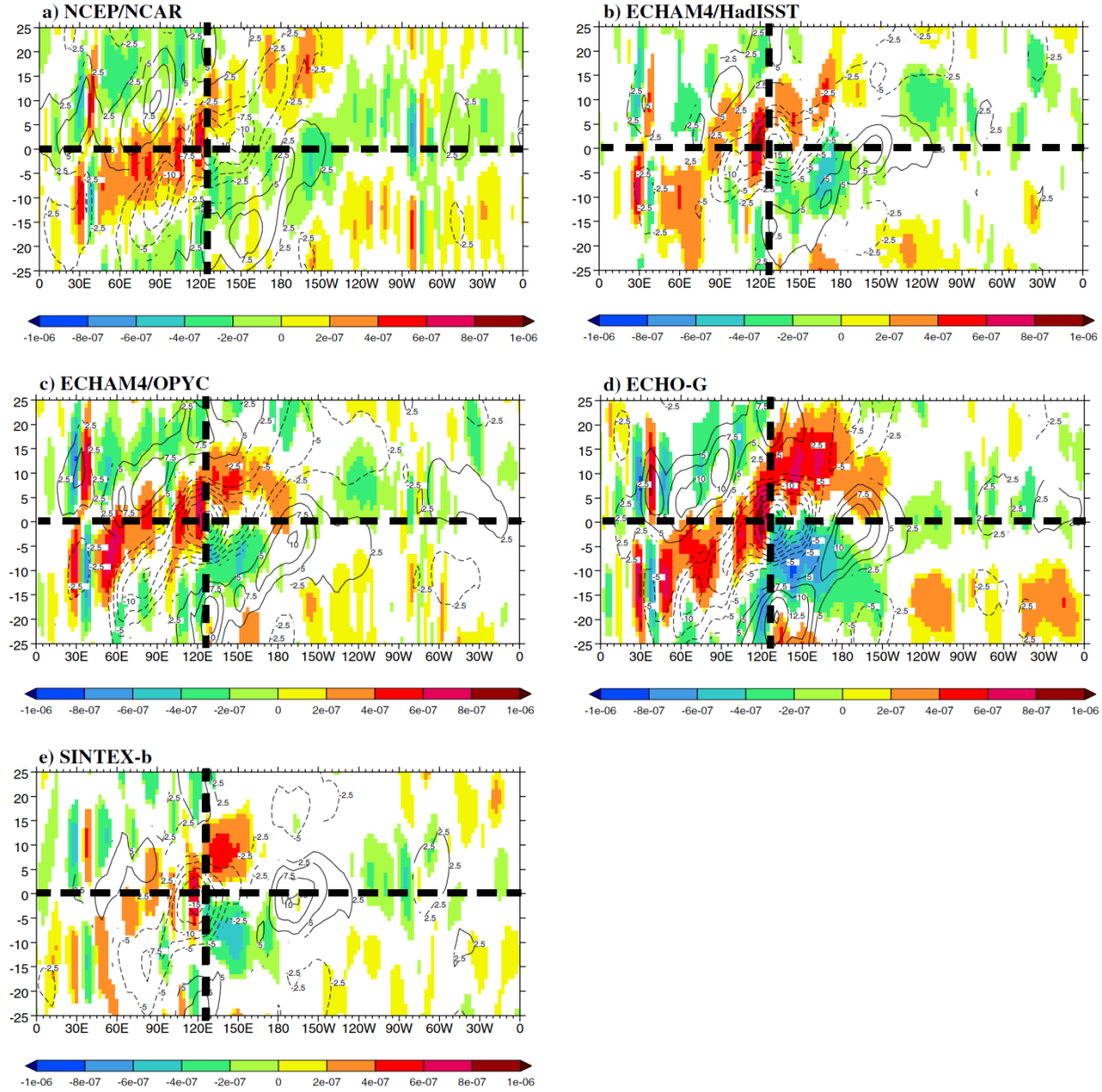


Fig. 13 Lag regression of PC-1 with 5°N–5°S averaged 20–100-day bandpass-filtered 1000 hPa divergence. a NCEP/NCAR, b ECHAM4/HadISST, c ECHAM4/OPYC, d ECHO-G, e SINTEX-b. The regressions have been scaled by a 1 SD perturbation of the respective PCs (Table 2) to give units of s^{-1} . Isolines of the OLR anomalies are also plotted at an interval of 2.5 Wm^{-2} . The vertical dashed line is the longitude of maximum convection at lag 0 (given by the horizontal dashed line). On the y-axis, the time lags are from -25 to 25 days

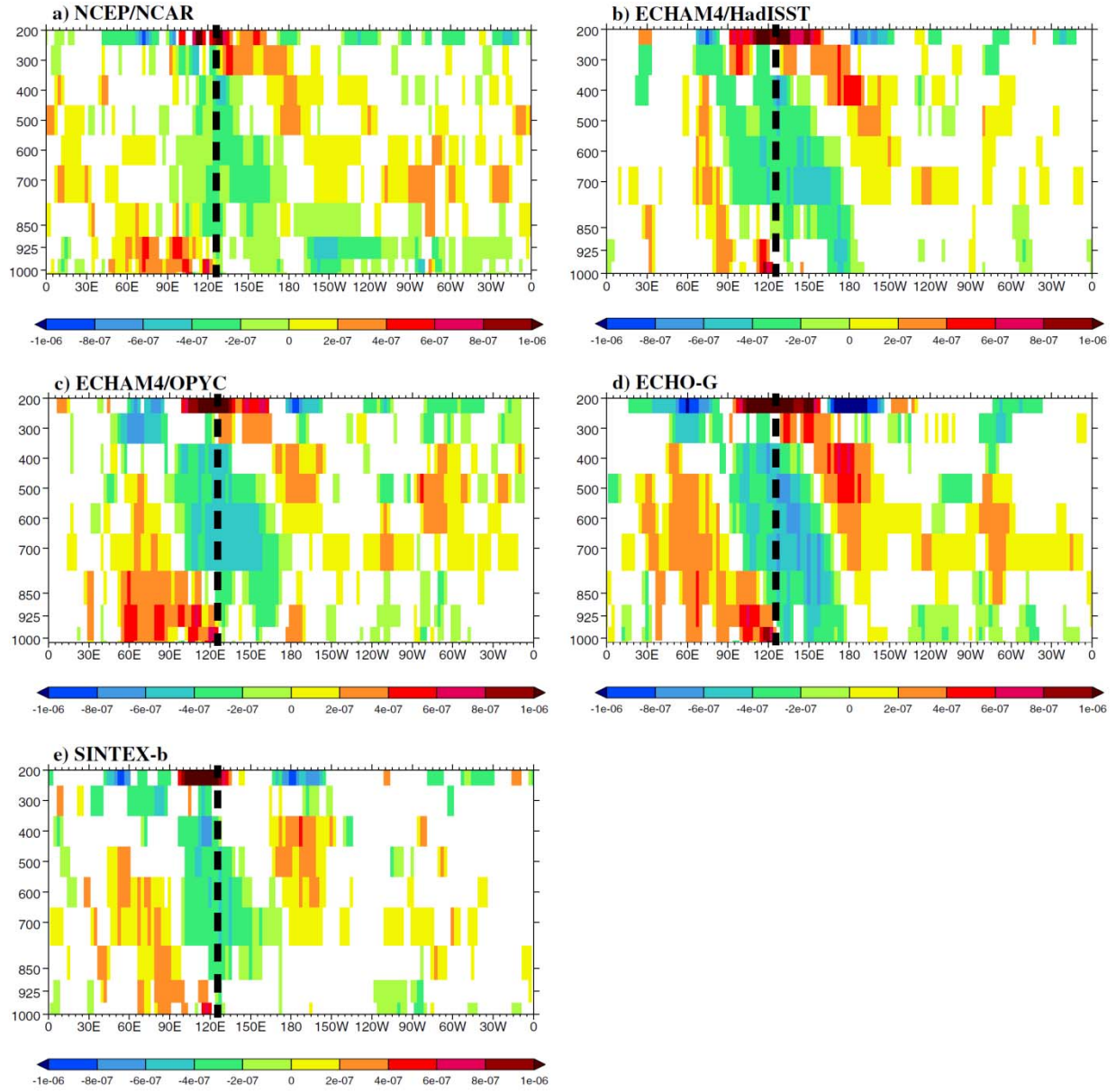


Fig. 14 Lag 0 regression of PC-1 with 5°N–5°S averaged 20–100-day bandpass-filtered divergence as a function of pressure level (hPa). a) NCEP/NCAR, b) ECHAM4/HadISST, c) ECHAM4/OPYC, d) ECHO-G, e) SINTEX-b. The regressions have been scaled by a 1 SD perturbation of the respective PCs (Table 2) to give units of s^{-1} . The vertical dashed line is the longitude of maximum convection at lag 0

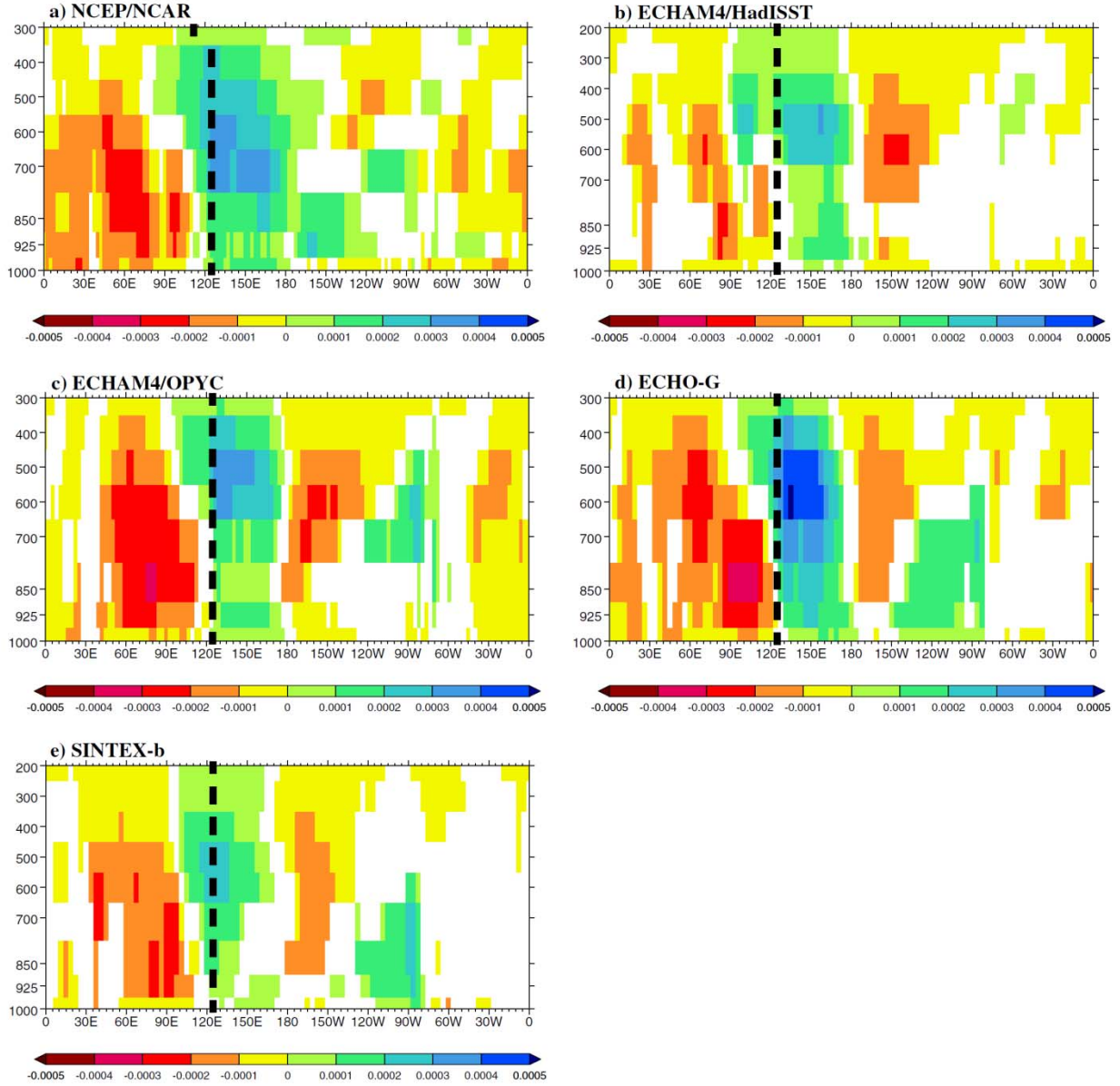


Fig. 15 Lag 0 regression of PC-1 with 5°N–5°S averaged 20–100-day bandpass-filtered specific humidity as a function of pressure level (hPa). a NCEP/NCAR, b ECHAM4/HadISST, c ECHAM4/OPYC, d ECHO-G, e SINTEX-b. The regressions have been scaled by 1 SD perturbation of the respective PCs (Table 2) to give units of kg kg⁻¹. The vertical dashed line is the longitude of maximum convection at lag 0

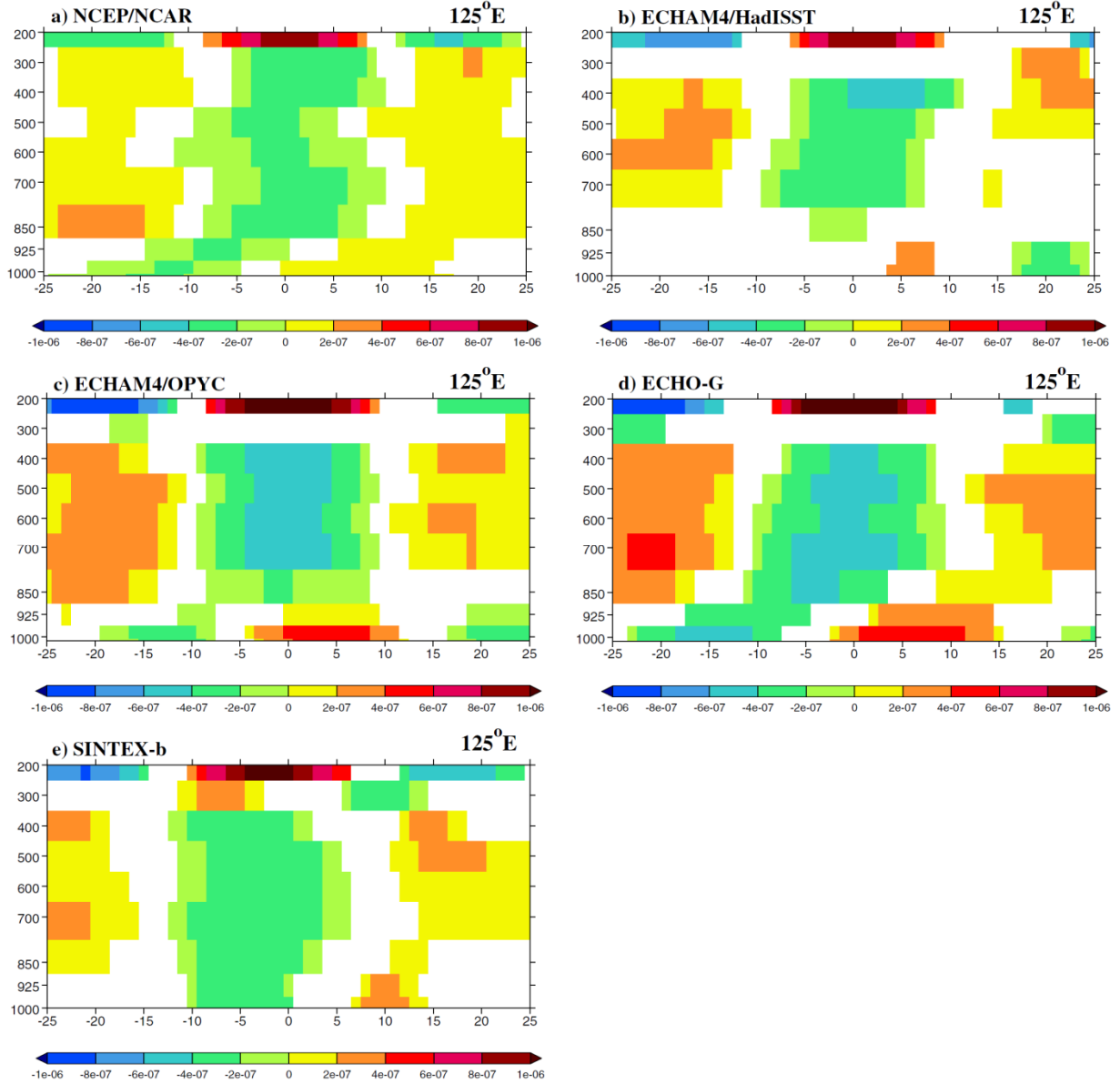


Fig. 16 Lag regressions (-25 to 25 days) of PC-1 with $5^{\circ}N$ – $5^{\circ}S$ averaged 20–100-day bandpass-filtered divergence as a function of pressure level (hPa). a NCEP/NCAR, b ECHAM4/HadISST, c ECHAM4/OPYC, d ECHO-G, e SINTEX-b. The regressions have been scaled by a 1 SD perturbation of the respective PCs (Table 2) to give units of s^{-1} . The longitude at which the vertical section is evaluated is given in the upper right-hand corner for each dataset

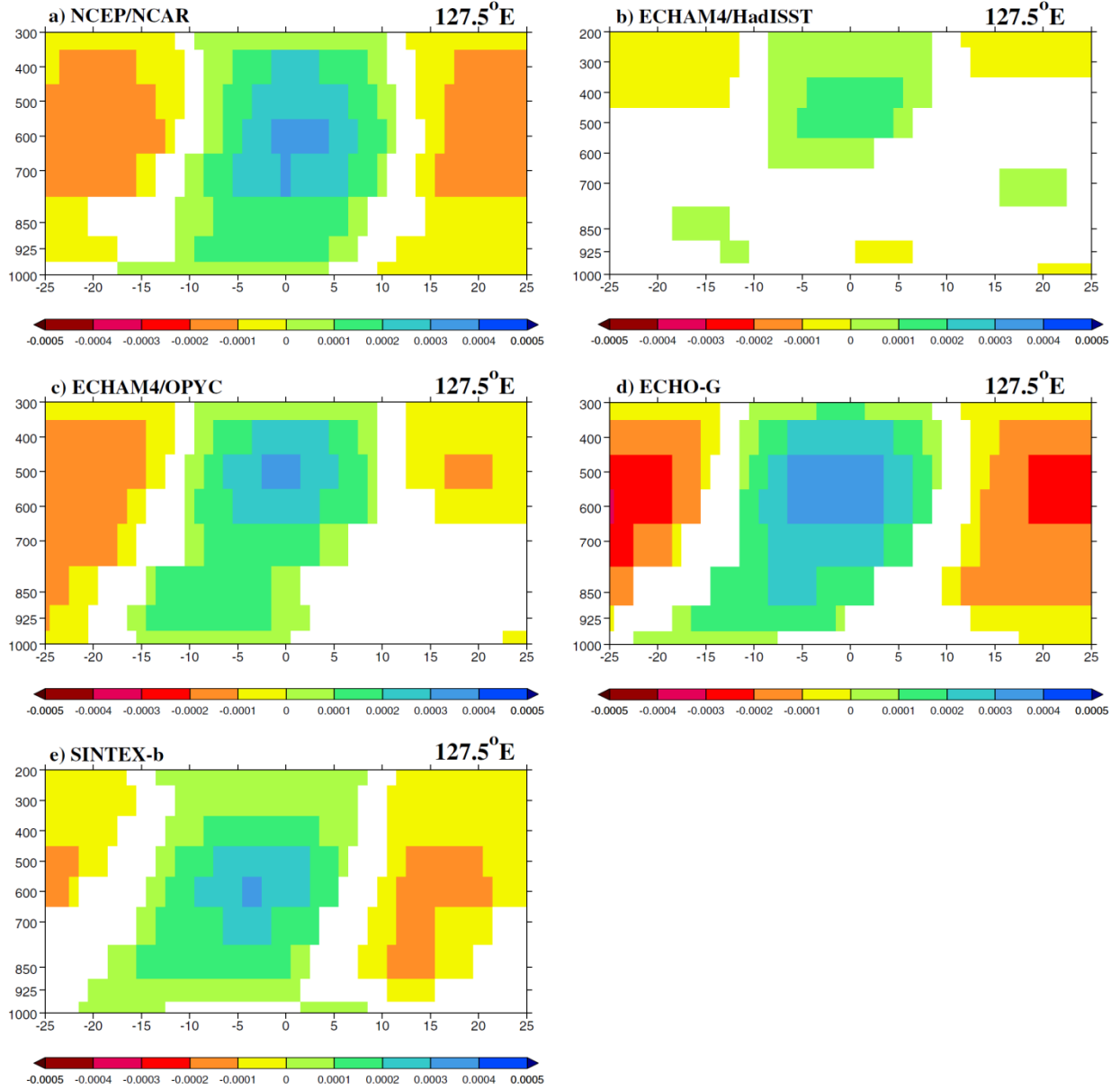


Fig. 17 Lag regressions (-25 to 25 days) of PC-1 with 5°N-5°S averaged 20–100-day bandpass-filtered specific humidity as a function of pressure level (hPa). (a) NCEP/NCAR, (b) ECHAM4/HadISST, (c) ECHAM4/OPYC, (d) ECHO-G, (e) SINTEX-b. The regressions have been scaled by a 1 SD perturbation of the respective PCs (Table 2) to give units of kg kg^{-1} . The longitude at which the vertical section is evaluated is given in the upper right-hand corner for each dataset